CELL MIGRATION

# Exocrine gland–resident memory CD8$^+$ T cells use mechanosensing for tissue surveillance

**Nora Ruef[1]†, Jose Martínez Magdaleno[1]†, Xenia Ficht[2], Vladimir Purvanov[3], Matthieu Palayret[1], Stefanie Wissmann[1], Petra Pfenninger[1], Bettina Stolp[4], Flavian Thelen[5], Juliana Barreto de Albuquerque[6], Philipp Germann[7], James Sharpe[7,8,9], Jun Abe[1], Daniel F. Legler[3,10,11], Jens V. Stein[1]***

Copyright © 2023 The Authors, some rights reserved; exclusive licensee American Association for the Advancement of Science. No claim to original U.S. Government Works

**Tissue-resident CD8$^+$ T cells ($T_{RM}$) continuously scan peptide-MHC (pMHC) complexes in their organ of residence to intercept microbial invaders. Recent data showed that $T_{RM}$ lodged in exocrine glands scan tissue in the absence of any chemoattractant or adhesion receptor signaling, thus bypassing the requirement for canonical migration-promoting factors. The signals eliciting this noncanonical motility and its relevance for organ surveillance have remained unknown. Using mouse models of viral infections, we report that exocrine gland $T_{RM}$ autonomously generated front-to-back F-actin flow for locomotion, accompanied by high cortical actomyosin contractility, and leading-edge bleb formation. The distinctive mode of exocrine gland $T_{RM}$ locomotion was triggered by sensing physical confinement and was closely correlated with nuclear deformation, which acts as a mechanosensor via an arachidonic acid and $Ca^{2+}$ signaling pathway. By contrast, naïve CD8$^+$ T cells or $T_{RM}$ surveilling microbe-exposed epithelial barriers did not show mechanosensing capacity. Inhibition of nuclear mechanosensing disrupted exocrine gland $T_{RM}$ scanning and impaired their ability to intercept target cells. These findings indicate that confinement is sufficient to elicit autonomous T cell surveillance in glands with restricted chemokine expression and constitutes a scanning strategy that complements chemosensing-dependent migration.**

## INTRODUCTION

CD8$^+$ T cell–mediated protection against viral infections hinges on the rapid detection of cognate peptide–major histocompatibility complex (pMHC) displayed on antigen-presenting and infected host cells. To expedite this process, CD8$^+$ T cells integrate biochemical cues from their microenvironment via chemoattractant and adhesion receptors (*1*). During an immune response, CD8$^+$ T cells adapt their adhesion and chemoattractant receptor expression pattern to their differentiation status. These expression patterns enable clonal selection in lymphoid organs, followed by elimination of infected cells in inflamed tissue and tissue surveillance in the memory phase (*2*). More specifically, naïve and central memory CD8$^+$ T cells ($T_N$ and $T_{CM}$, respectively) express CD62L and CCR7 for homing to secondary lymphoid organs (SLOs), whereas effector and effector memory T cells ($T_{EFF}$ and $T_{EM}$, respectively) display high surface levels of inflammatory chemokine and adhesion receptors to enter nonlymphoid tissues. Chemokine and adhesion receptors are also critical for interstitial scanning within target organs, the prerequisite for antigen-specific protection afforded by $T_{EFF}$ (*3*–*5*). Last, tissue-resident memory T cells ($T_{RM}$) express numerous chemokine and adhesion receptors including CXCR3, CXCR6, CD49a, and CD103, which contribute to their long-term persistence in their tissue of residence and to the surveillance of epithelial barriers exposed to microbes (*6*–*13*).

Their vigorous scanning behavior makes CD8$^+$ T cells a valuable model to study amoeboid cell migration, a heterogeneous phenomenon encompassing forward and retrograde F-actin flow, as well as different types of protrusions such as lamellipodia, pseudopods, and blebs (*14*–*19*). Recent studies have dissected the precise mode of amoeboid migration of $T_N$. These cells generate a CCR7-driven retrograde cortical F-actin flow dependent on the guanine exchange factor (GEF) DOCK2 and its downstream targets Rac1 and Rac2 (*20*–*23*). Retrograde F-actin flow transmits weak forces via the integrin LFA-1 to its receptor intercellular adhesion molecule–1 (ICAM-1) displayed on stromal cells, providing the traction force for rapid $T_N$ locomotion within the lymphoid parenchyma without inducing substantial adhesion (*23*–*25*).

In addition to the paradigmatic T cell migration driven by chemosensing of external cues, we have recently uncovered a distinct motility signature displayed by submandibular salivary gland (SMG) CD8$^+$ $T_{RM}$ (*26*). Although these cells exhibit high in vivo migration speeds of 6 to 7 μm/min, we did not find evidence for a substantial contribution for chemoattractant and adhesion receptors during homeostatic organ surveillance because neither pertussis toxin treatment (to block $G_{\alpha i}$-coupled receptors) nor integrin inhibition influenced their motility. Instead, SMG CD8$^+$ $T_{RM}$ spontaneously migrate with frequent shape changes in the absence of chemoattractants and specific adhesive interactions (*26*), perhaps as an adaptation to the chemokine-poor milieu of noninflamed salivary glands (*27*). This is in contrast to epidermal CD8$^+$ $T_{RM}$, which require external chemoattractants for motility (*8*, *26*). In line with our

[1]Department of Oncology, Microbiology and Immunology, University of Fribourg, 1700 Fribourg, Switzerland. [2]Department of Biosystems Science and Engineering, ETH Zürich, Mattenstrasse 22, 4058 Basel, Switzerland. [3]Biotechnology Institute Thurgau (BITg) at the University of Konstanz, 8280 Kreuzlingen, Switzerland. [4]Department for Infectious Diseases, Integrative Virology, Center for Integrative Infectious Disease Research, University Hospital Heidelberg, 69120 Heidelberg, Germany. [5]Department of Medical Oncology and Hematology, University of Zürich and University Hospital Zürich, 8091 Zürich, Switzerland. [6]Division of Experimental Pathology, Institute of Pathology, University of Bern, 3008 Bern, Switzerland. [7]Centre for Genomic Regulation (CRG), Barcelona Institute of Science and Technology (BIST), 08003 Barcelona, Spain. [8]European Molecular Biology Laboratory (EMBL) Barcelona, 08003 Barcelona, Spain. [9]Institucio' Catalana de Recerca i Estudis Avancats (ICREA), 08010 Barcelona, Spain. [10]Faculty of Biology, University of Konstanz, 78464 Konstanz, Germany. [11]Theodor Kocher Institute, University of Bern, 3011 Bern, Switzerland.
*Corresponding author. Email: jens.stein@unifr.ch
†These authors contributed equally to this work.

Downloaded from https://www.science.org at Harvard University on January 04, 2024

findings, T cell lines can migrate in complete absence of chemokine and adhesion receptors using topography-dependent force transmission (*28*). However, the cues that trigger receptor-independent motility of $CD8^+$ $T_{RM}$ lodging in resting glands and the relevance of this noncanonical migration to intercept Ag-presenting cells remain unknown to date.

Here, we have systemically compared SMG $T_{RM}$ motility with the canonical chemosensing-driven $T_N$ amoeboid migration. In the absence of external biochemical cues, $T_{RM}$ spontaneously generated retrograde F-actin flow as a force-generating module for translocation. Furthermore, $T_{RM}$ displayed a highly contractile actomyosin cytoskeleton, leading to continuous bleb formation at the leading edge. Autonomous cell motility was also observed in lacrimal gland (LG) $T_{RM}$ but not $T_N$ or small intestine (SI) $T_{RM}$, and this was strictly dependent on their ability to sense and react to mechanical load of their microenvironment. Mechanosensing triggered an "evasion reflex," which elicited cortical actomyosin contractility through arachidonic acid (AA) and intracellular $Ca^{2+}$ signaling and correlated with nuclear deformation, in line with the recently uncovered function of the nucleus as mechanosensor in mammalian and nonmammalian cells (*29*, *30*). Inhibition of mechanosensing signaling disrupted $T_{RM}$ tissue scanning and interception of target cells. Our data suggest that memory T cells lodged in organs with low microbial exposure have co-opted a conserved mechanosensory module for immunosurveillance, suggesting an instructive role for physical confinement to elicit dynamic T cell motility. In combination with their preserved chemosensing capacity, our data identify a multitier strategy for $T_{RM}$-mediated tissue surveillance. Such a strategy bypasses the requirement for elevated constitutive chemokine and adhesion receptor expression in resting nonbarrier tissues, thus preventing unwarranted leukocyte influx.

## RESULTS

### SMG $T_{RM}$ spontaneously generate retrograde F-actin flow in the absence of chemoattractants and specific adhesions

Our previous in vivo and ex vivo analysis uncovered high intrinsic SMG $CD8^+$ $T_{RM}$ motility (movie S1), which bypasses canonical chemoattractant sensing and adhesion receptor engagement (*26*). To generate SMG $CD8^+$ $T_{RM}$ for an in-depth examination of the underlying actomyosin cytoskeleton regulation, we adoptively transferred congenically marked OT-I T cell receptor (TCR) transgenic $CD8^+$ T cells, which recognize the ovalbumin (OVA) peptide $OVA_{257–264}$ in the context of H-$2K^b$ (*31*), into C57BL/6 mice. One day later, recipient mice were infected with lymphocytic choriomeningitis virus–OVA (LCMV-OVA), a replication-competent, attenuated LCMV variant encoding OVA as model antigen (Fig. 1A) (*32*). Although rapidly cleared, LCMV-OVA infection results in OT-I expansion and formation of $T_{CM}$ and $T_{EM}$ populations in the spleen and lymph nodes (LNs) and bona fide $CD103^+$ $T_{RM}$ in SMGs at ≥30 days post infection (p.i.) (fig. S1A). Cell sizes were similar between $T_N$ and endogenous or adoptively transferred $CD8^+$ $T_{EM}$ and $T_{RM}$, whereas $T_{CM}$ showed a tendency toward increased cell size (fig. S1B). Similarly, levels of the F-actin regulators phospho-cofilin and DOCK2 were not elevated in $T_{RM}$ as compared to other memory subsets, and the expression and phosphorylation of ezrin-radixin-moesin (ERM) proteins, which link cortical F-actin to the plasma membrane, remained unchanged (fig. S1, C to F). In contrast, both endogenous and adoptively transferred SMG $CD8^+$ $T_{RM}$ contained higher F-actin levels as compared with other T cell subsets (Fig. 1B).

We used the F-actin probe LifeAct-GFP (green fluorescent protein) to examine steady-state actin cytoskeleton dynamics in $T_{RM}$ (*33*). We generated LifeAct-$GFP^+$ SMG OT-I $T_{RM}$ as above and compared their cortical actin cytoskeleton dynamics with LifeAct-$GFP^+$ $T_N$ as a well-characterized benchmark using total internal reflection fluorescence (TIRF) microscopy in an under-agarose system (*23*, *34*–*36*). Under-agarose assays create promigratory conditions in the absence of a directional chemokine gradient, thus mimicking the random guided walk characteristic of $T_N$ in lymphoid tissue and the homeostatic surveillance of $T_{RM}$ in SMGs (*23*, *26*, *37*). Initially, we measured F-actin flow without cellular translocation by placing $T_N$ and $T_{RM}$ onto "slippery" surfaces passivated with Pluronic F-127 (pluronic), a nonionic surfactant polyol. This approach permits the quantification of cortical F-actin flow speeds during spontaneous or chemokine-induced F-actin treadmilling. In the absence of chemokines, $T_N$ contained only sparse and short-lived cortical F-actin dots correlating with their unpolarized phenotype (Fig. 1, C and D, and movie S2). To assess the impact of biochemical stimulation on F-actin dynamics, we added CCL19 as a ligand for the $T_N$-expressed chemokine receptor CCR7. CCL19 rapidly induced cortical F-actin filaments that flowed from the leading to the trailing edge with speeds of 14.5 ± 8.2 μm/min (mean ± SD; Fig. 1, C and D). This resulted in a "running on the spot" phenotype on pluronic-passivated surfaces (movie S2). When CCL19-stimulated $T_N$ were plated on ICAM-1–coated plates, retrograde F-actin flow was converted into fast chemokinetic cell movement by force-coupling of LFA-1 to ICAM-1 as described (Fig. 1, C and D, and movie S2) (*23*). This was accompanied by the stalling of net rearward F-actin flow, with LifeAct-$GFP^+$ F-actin becoming stationary in relation to the substrate (Fig. 1D).

In contrast to $T_N$, LifeAct-$GFP^+$ SMG $T_{RM}$ plated on pluronic-passivated surfaces showed intrinsic cortical F-actin treadmilling from the front to the rear with speeds of 9.7 ± 6.8 μm/min (Fig. 1, C and D), resulting in a polarized phenotype. This was accompanied by frequent F-actin protrusion formation at the leading edge (movie S3). Thus, SMG $T_{RM}$ not only contain more total F-actin but also exhibit a continuous front-to-back flow of F-actin filaments even in the absence of biochemical cues (i.e., chemokines). To assess the impact of chemokines on F-actin flow, we added CXCL10, the ligand for the $T_{RM}$-expressed chemokine receptor CXCR3, because these cells do not express CCR7. Whereas the speed of retrograde cortical F-actin flow was accelerated to 12.8 ± 8.5 μm/min upon CXCL10 exposure, the increase was lower than for chemokine-stimulated $T_N$ (Fig. 1, C and D, and movie S3). Front-to-back F-actin flow stalled when $T_{RM}$ were placed on lipid-free human serum albumin (HSA), which provides sufficient friction to generate traction force for cell translocation, in the absence of specific adhesive interactions (Fig. 1, C and D, and movie S3) (*26*). In addition, we observed occasional forward movement of F-actin filaments at the trailing edge (Fig. 1C, dashed line). This observation is indicative of a highly contractile uropod, which drags F-actin filaments toward the leading edge (*38*). In sum, $T_{RM}$ use retrograde cortical F-actin flow for translocation akin to the cortical flow-force transmission model described for motile $T_N$ (*23*, *39*). Unlike $T_N$, cortical F-actin flow in $T_{RM}$ is induced spontaneously in the absence of external chemoattractants. Nonetheless, our data confirm that SMG $T_{RM}$ remain responsive to CXCL10. This is in line with previous observations that $CXCR3^{-/-}$ $T_{RM}$ do not accumulate around tissue macrophage clusters in vivo despite scanning salivary gland parenchyma with speeds comparable to wild-type (WT) $T_{RM}$ (*26*).

Downloaded from https://www.science.org at Harvard University on January 04, 2024

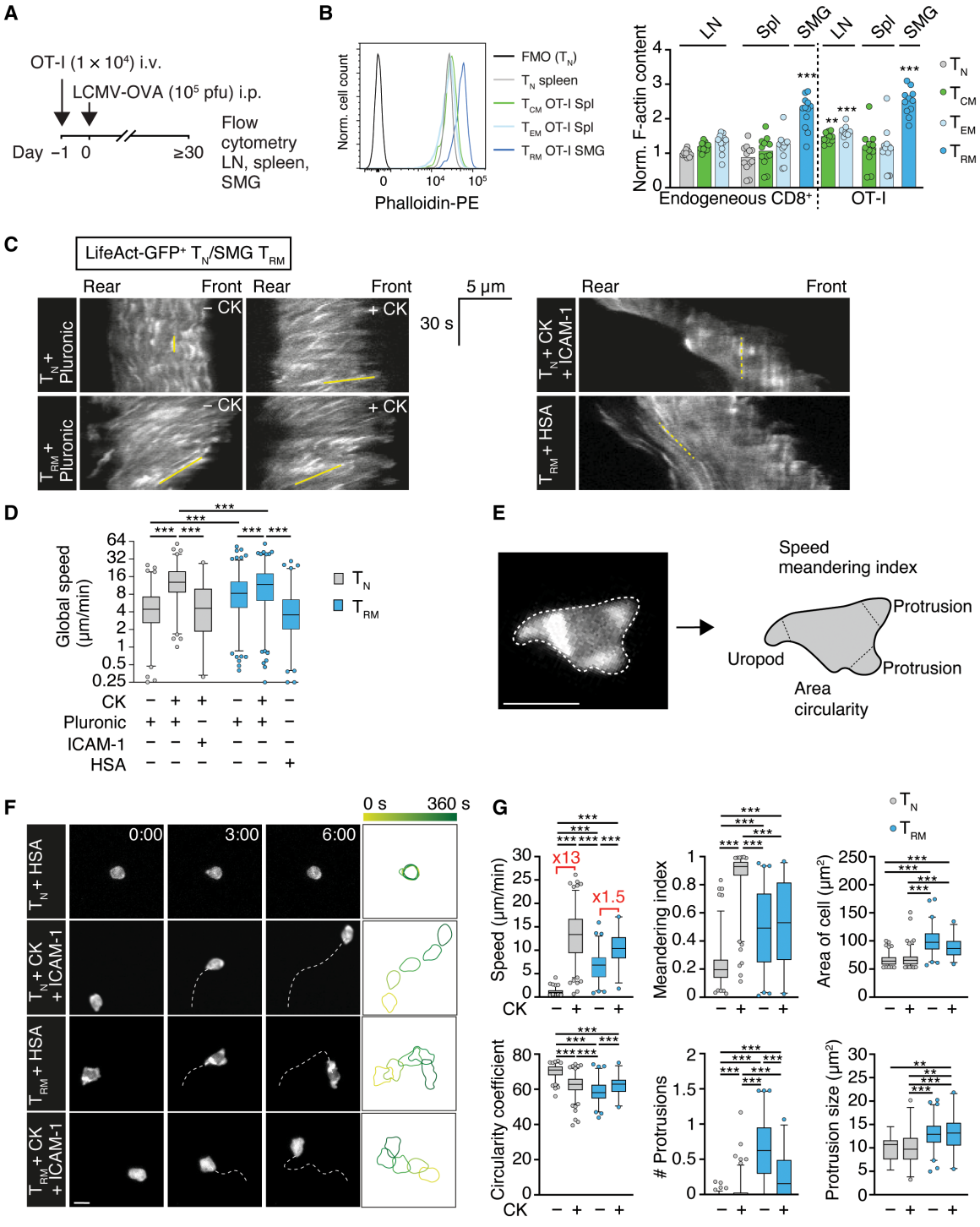


**Fig.1. SMG $T_{RM}$ autonomously generate F-actin flow for chemokine- and specific adhesion–independent amoeboid motility.** (**A**) Experimental layout. (**B**) Flow cytometry plots and quantification of F-actin content in LN and spleen (Spl) $T_N$, $T_{CM}$, $T_{EM}$, and SMG $T_{RM}$. Bars represent median. (**C**) TIRF images of cortical F-actin flow in LifeAct-GFP$^+$ $T_N$ and SMG $T_{RM}$ under agarose. Note that for $T_N$ plated in the absence of chemokine (–CK), there is no front or rear discernible because these cells are non-polarized. Yellow lines indicate rearward (continuous) and forward (dotted) F-actin flow. CK, chemokine. (**D**) Global F-actin flow speeds in $T_N$ and SMG $T_{RM}$. (**E**) Schematic layout of dynamic and morphometric analysis. Scale bar, 10 µm. (**F**) Wide-field fluorescence microscopy images of $T_N$ and SMG $T_{RM}$ under agarose migration. Time in min:s. Scale bar, 10 µm. (**G**) Dynamic and morphometric analysis of $T_N$ and SMG $T_{RM}$ displacement. Red numbers indicate fold change. Data in (B and G) were pooled from at least two independent experiments with $n = 11$ or 12 mice (B) and $n = 60$ to 279 tracks per condition (G), and (D) is from one of two representative experiments with 21 to 24 cells per condition and $n = 411$ to 777 individual F-actin spots tracked per condition (except $T_N$ + CK on ICAM-1: 144 F-actin spots). Statistical analysis was done by a Kruskal-Wallis test against LN $T_N$ (B) or between all columns (D and G). $^{**}P < 0.01$ and $^{***}P < 0.001$.

Downloaded from https://www.science.org at Harvard University on January 04, 2024

### Morphometric analysis uncovers high protrusion formation in spontaneously migrating SMG $T_{RM}$

We compared the amoeboid motility modes of $T_N$ and $T_{RM}$ in more detail by examining displacement parameters in combination with a morphometric (i.e., cell shape) analysis. To this end, we used wide-field fluorescence microscopy of T cells under agarose (without pluronic passivation) and determined cell speeds, meandering index, cell area, and circularity, as well as numbers and sizes of leading edge protrusions using a customized analysis pipeline (Fig. 1E and fig. S2). We first compared $T_N$ motility on HSA without CCL19 (as a nonmigratory substrate) to ICAM-1 + CCL19–coated plates to mirror conditions used for F-actin flow measurements (*23*). In agreement with F-actin dynamics identified by TIRF microscopy (Fig. 1C), $T_N$ converted from a nonmotile state with rounded cell morphology in the absence of chemokines and adhesive ligands to a polarized phenotype with high speeds and directionality when ICAM-1 and CCL19 were present (from 1.2 ± 0.5 to 13.1 ± 4.8 μm/min; Fig. 1, F and G, and movie S4). $T_N$ speeds closely matched CCL19-triggered rearward F-actin flow speeds under slippery conditions (Fig. 1G), suggesting that the F-actin flow is efficiently converted into forward movement on ICAM-1–coated substrates. Irrespective of the presence or absence of CCL19, $T_N$ formed very few protrusions (Fig. 1G, bottom middle panel).

In line with TIRF measurements, $T_{RM}$ acquired a spread and polarized shape with numerous protrusions and spontaneously moved on HSA-coated plates, even in the absence of chemokines and specific adhesive substrates (Fig. 1, F and G). We then examined the impact of chemokine addition in the presence of ICAM-1 coating to recreate similar promigratory conditions as used for $T_N$. Whereas ligands for the $T_{RM}$-expressed chemokine receptors CXCR3 and CXCR4 together with ICAM-1 were associated with increased SMG $T_{RM}$ speeds (from 6.7 ± 3.0 to 10.5 ± 3.1 μm/min), the increase was less pronounced than in $T_N$ (Fig. 1G and movie S5). Furthermore, chemokine exposure did not increase $T_{RM}$ directionality (as assessed by the meandering index), in contrast to $T_N$ (Fig. 1G). Instead, chemokines reduced protrusion formation in $T_{RM}$ (Fig. 1G). Together, autonomously moving $T_{RM}$ display a protrusion-rich amoeboid migration phenotype, which is distinct from the well-characterized $T_N$ mode (*23*). Our data are in line with a model in which protrusion formation does not translate into fast leukocyte motility (*38*) but is instead driven by retrograde F-actin flow and force coupling to substrate (*23*, *39*).

### Constitutive DOCK2-Rac-Arp2/3 signaling is required for autonomous SMG $T_{RM}$ motility

Retrograde F-actin flow can be generated by F-actin polymerization at the leading edge and/or by Rho-mediated contraction of the F-actin network (*22*, *40*–*42*), so we used under-agarose assays to explore the roles for Rac and Cdc42 as major drivers of Arp2/3-mediated F-actin generation at the leading edge (fig. S3A) (*43*). Reflecting the accumulation of the Rac GEF DOCK2 at the leading edge of migrating $T_{RM}$ (fig. S3B), the DOCK2 inhibitor CPYPP (*44*) and CK666, an inhibitor of the DOCK2-Rac downstream target Arp2/3 (*45*), decreased speed, meandering index, and protrusion formation in SMG $T_{RM}$, with a concomitant increase in circularity and a decrease in cell area (fig. S3, C and D, and movie S6). Similarly, inhibition of Rac1 using the W56 peptide inhibited autonomous $T_{RM}$ motility (fig. S3, E and F). In contrast, the Cdc42 inhibitor ML141 did not alter $T_{RM}$ speeds and circularity, although it caused a trend to a lower meandering index and a minor decrease in cellular area and average protrusion size (fig. S3, C and D). To corroborate the roles for Rac-driven versus Cdc42-driven $T_{RM}$ motility in vivo, we adoptively transferred WT $tdTom^+$ and $GFP^+$ OT-I T cells lacking DOCK2 or the Cdc42 GEF DOCK8 into C57BL/6 recipients 1 day before infection with LCMV-OVA. Although DOCK2 deficiency impairs T cell accumulation in nonlymphoid tissues (*46*), we were able to identify occasional $DOCK2^{-/-}$ $T_{RM}$ at >30 days p.i. within SMGs. Intravital imaging confirmed strongly reduced cell speeds and directionality in the absence of DOCK2 as compared with WT $T_{RM}$ (fig. S3, G and H, and movie S7). DOCK8 has previously been shown to mediate T cell migration in skin (*47*). In contrast, $DOCK8^{-/-}$ SMG $T_{RM}$ moved with comparable speeds as WT $T_{RM}$, with only a minor reduction in directionality (fig. S3I). These data support a central role for leading edge DOCK2-Rac-Arp2/3–driven F-actin polymerization for SMG $T_{RM}$-mediated tissue surveillance.

### SMG $T_{RM}$ have high constitutive actomyosin contractility

We next examined the role of actomyosin contractility for spontaneous SMG $T_{RM}$ motility. Non-muscle myosin IIA (MYH9)–mediated contractility of F-actin filaments supports amoeboid cell motility by pulling F-actin filaments toward the trailing edge and by generating force to push the nucleus as the biggest organelle through narrow pores (*48*). Using a reporter line expressing GFP-tagged myosin IIA under the endogenous *Myh9* promoter (*49*), we observed notably higher MYH9-GFP levels in SMG OT-I $T_{RM}$ as compared with $T_{CM}$ and $T_{EM}$, suggesting a high baseline contractility (Fig. 2A). In under-agarose assays, MYH9-GFP accumulated mostly at the trailing edge of migrating SMG $T_{RM}$ (Fig. 2B and movie S8), consistent with local F-actin contractions observed in TIRF imaging (Fig. 1C). MYH9-GFP also accumulated in protrusions of the leading edge, followed by their subsequent retraction (Fig. 2B). This observation points to a dual role for myosin IIA activity: first, to contract the uropod and, second, to retract protrusions that are not aligned with the migratory path, as described for neutrophils (*50*). In line with elevated MYH9 expression, SMG $T_{RM}$ contained two to three times higher phosphorylated myosin light chain (pMLC) levels as compared with $T_{CM}$ and $T_{EM}$ (Fig. 2, C and D).

We next attempted to genetically assess MYH9 function for SMG $T_{RM}$ scanning but failed to obtain MYH9-deficient peripheral T cells in a CD4-Cre × $MYH9^{fl/fl}$ line (fig. S4A). Similarly, Cas9-mediated MYH9 depletion resulted in defective OT-I T cell expansion after viral infection, in line with its role in cytokinesis (fig. S4, B and C) (*51*). We therefore performed under-agarose assays in the presence of selected inhibitors of the MLC phosphorylation cascade (Fig. 2E). Direct inhibition of Rho using rhosin decreased SMG $T_{RM}$ speeds and protrusion sizes (fig. S5, A and B). We next evaluated its downstream effectors, MLC kinase (MLCK) and Rho-associated coiled-coil kinase (ROCK), both of which regulate pMLC levels. MLCK inhibition slightly reduced $T_{RM}$ speeds (from 7.1 ± 3.7 to 5.4 ± 3.0 μm/min; mean ± SD) but did not significantly alter directionality, cell shape and area, or protrusion formation (Fig. 2, F and G, and movie S9). In contrast, the ROCK inhibitor Y-27632 caused cell rounding and a substantial decrease in speeds to 0.7 ± 2.7 μm/min, as well as low directionality and protrusion formation (Fig. 2, F and G, and movie S9). Furthermore, Y-27632 blocked topography-driven $T_{RM}$ motility on pluronic-passivated surfaces (fig. S5, C and D), as well as SMG $T_{RM}$ surveillance in situ as assessed by intravital

Downloaded from https://www.science.org at Harvard University on January 04, 2024

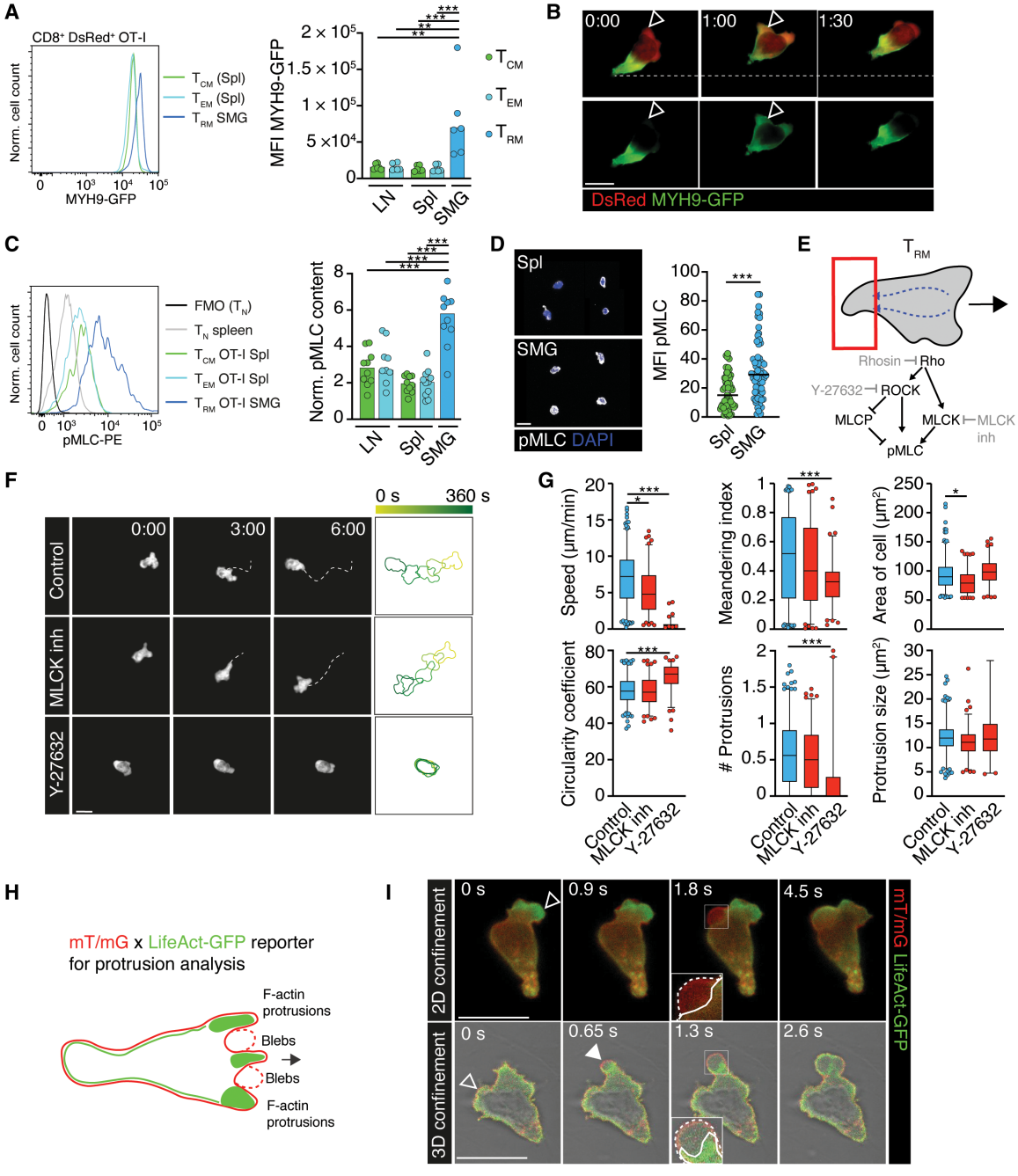


**Fig. 2. SMG $T_{RM}$ display high constitutive actomyosin contractility and bleb formation during spontaneous migration.** (**A**) Flow cytometry analysis of MYH9-GFP–expressing $T_{CM}$, $T_{EM}$, and SMG $T_{RM}$ DsRed$^+$ OT-I T cells. (**B**) MYH9-GFP dynamics in DsRed$^+$ OT-I T cells under agarose migration. Empty arrowheads indicate DsRed$^+$ leading edge protrusions. The bottom row depicts MHY-GFP signal only. Time in min:s. Scale bar, 10 µm. (**C**) Flow cytometry analysis of pMLC in endogenous $T_N$ and OT-I $T_{CM}$, $T_{EM}$, and SMG $T_{RM}$. (**D**) Immunofluorescent analysis of pMLC in spleen and SMG memory OT-I T cells. (**E**) Scheme of Rho-triggered pMLC generation and selected inhibitors. (**F**) Wide-field fluorescence microscopy images of SMG $T_{RM}$ under agarose migration in the presence of inhibitors. Time in min:s. Scale bar, 10 µm. (**G**) Dynamic and morphometric analysis of SMG $T_{RM}$ displacement. (**H**) Scheme of F-actin–filled protrusion versus bleb formation in migrating LifeAct-GFP × mT/mG SMG $T_{RM}$. (**I**) High temporal resolution protrusion analysis of migrating LifeAct-GFP × mT/mG SMG $T_{RM}$ OT-I under 2D and 3D confinement. Empty arrowheads indicate F-actin–filled protrusions; filled arrowheads indicate blebs. Inserts depict blebs defined by a separation of the mT/mG signal (dotted line) from the LifeAct-GFP signal (continuous line). Scale bars, 10 µm. Bars in (A) and (C) represent medians. Data in (A) ($n = 6$ mice), (C) ($n = 9$ to 11 mice), (D) ($n = 63$ to 65 cells), and (G) ($n = 184$ to 239 tracks) were pooled from at least two independent experiments and analyzed by ANOVA (A and C), Mann-Whitney test (D), or a Kruskal-Wallis test against control (G). *$P < 0.05$, **$P < 0.01$, and ***$P < 0.001$.

imaging (fig. S5E). Because Rho–guanosine triphosphate activates nucleation factors of the formin/mDia family, we performed under-agarose assays in the presence of the formin homology 2 domain inhibitor SMIFH2. We observed decreased $T_{RM}$ speeds, directionality, protrusion formation, and cell area in the presence of this inhibitor (fig. S5, F and G). As a caveat, SMIFH2 has been reported to

Downloaded from https://www.science.org at Harvard University on January 04, 2024

affect additional factors including MYH9 (*52*, *53*). In sum, SMG $T_{RM}$ have high intrinsic actomyosin contractility, which is required for inherent motility and organ surveillance.

### $T_{RM}$ form blebs at the leading edge during two-dimensional and three-dimensional space exploration

High baseline actomyosin contractility leads to increased intracellular hydrostatic pressure that can cause blebs, short-lived F-actin–free membrane protrusions (*16*) (*54*) (*55*). To unequivocally assess whether SMG $T_{RM}$ displayed bleb formation during migration, we generated LifeAct-GFP × mT/mG OT-I T cells, in which F-actin and plasma membrane are tagged with GFP and tdTom, respectively (Fig. 2H). We transferred LifeAct-GFP × mT/mG OT-I into recipient C57BL/6 mice, followed by LCMV-OVA infection and sorting of SMG $T_{RM}$ in the memory phase. High–frame rate in vitro imaging confirmed the presence of two types of leading-edge protrusions: F-actin–filled protrusions and membrane blebs, which were rapidly (<1 s) filled with F-actin (Fig. 2I and movie S10). This correlated with quick accumulation of DOCK2 into blebs (movie S10). We did not find evidence for the formation of thin lamellipodia observed in lymphoblasts migrating on adhesive two-dimensional (2D) surfaces (*56*), perhaps owing to the low adhesiveness of HSA and the substantially lower amount of cytoplasm in resting versus activated T cells (*57*). Both F-actin–filled protrusions and blebs were short-lived and restricted to the leading edge of motile $T_{RM}$ because they were followed either by the translocation of the cell body or by retraction. Last, we also detected F-actin–filled protrusions and rapid bleb formation that bulged out into the extracellular space at the front of $T_{RM}$ moving in 3D collagen matrices, occasionally followed by the bulky nucleus (Fig. 2I and movie S10). Bleb-supported migration is therefore suited to rapid exploration of the available space in front of the cell's leading edge. Alternatively or in addition, blebs might contribute to motility and cell survival (*17*, *58*). Together, motile $T_{RM}$ and $T_N$ differ in two key features. First, rearward F-actin flow in $T_{RM}$ is generated even without external guidance cues. Second, $T_{RM}$ have high intrinsic actomyosin contractility correlating with formation of blebs and F-actin–filled protrusions.

### Exocrine gland $T_{RM}$ use mechanosensing to trigger polarization and motility

We next explored the cellular and molecular mechanism underlying autonomous SMG $T_{RM}$ motility. Previous studies have shown that activated T cells migrate rapidly on 2D surfaces without confinement (*59*). Furthermore, nonattached leukocytes can use rearward F-actin treadmilling or myosin II–dependent membrane flow for fast translocation (*60*, *61*). To test whether this also applies to SMG $T_{RM}$, we examined their migration dynamics on 2D surfaces without agarose overlay, anticipating that these highly contractile cells would continue to display a polarized phenotype and motility (Fig. 3A). However, most $T_{RM}$ lost their polarized cell shape and created fewer protrusions on 2D surfaces than spatially confined cells did (Fig. 3, B to D). As a result, $T_{RM}$ displacement was essentially abolished under these conditions (Fig. 3, C and D). Thus, $T_{RM}$ need spatial confinement to acquire a polarized phenotype and for translocation.

To further delineate the relationship between spatial confinement, cell morphometry, and autonomous motility, we exposed SMG $T_{RM}$ to distinct mechanical loads. We adjusted the agarose concentration from 0.5% (corresponding to a Young's modulus of 2.9 kPa) to 1% (9.8 kPa) as described (*23*). We found that $T_{RM}$ responded to the degree of mechanical load with changes in cell shape, protrusion formation, and motility parameters. When exposed to higher mechanical load (1% agarose), $T_{RM}$ slowed down, moved less directionally, were less polarized, and formed fewer protrusions. These data are consistent with a model in which the forces required to lift agarose for protrusion formation and cell motility increase under high mechanical load, resulting in reduced cell migration. We then analyzed $T_{RM}$ motility exposed to 0.125 and 0.25% agarose, assuming that reduction of the environmental resistance to deformation facilitates cell motility. We found that under conditions of reduced mechanical load, $T_{RM}$ moved more slowly, were more spherical, and formed fewer and smaller protrusions than observed with 0.5% agarose (Fig. 3, E and F). Thus, $T_{RM}$ react to the degree of confinement using a mechanosensing module.

Next, we examined whether mechanosensing was a property shared with $T_{RM}$ from other internal organs. To address this point, we isolated $T_{RM}$ from another exocrine gland, the LG, or from the epithelial barrier of the SI after LCMV-OVA infection. In under-agarose assays, LG but not SI $T_{RM}$ displayed confinement-induced motility akin to SMG $T_{RM}$ (Fig. 3, G and H). In combination with the observation that epidermal $T_{RM}$ do not respond to physical confinement (*26*), these data suggest that exocrine gland but not skin or gut $T_{RM}$ have acquired the ability to mechanosense their environment, thus being able to measure and respond to a mechanical load with gradual induction of polarity and cell motility.

### Confinement-induced $T_{RM}$ motility requires nuclear mechanosensing-triggered signaling pathways

We explored the mechanism underlying cellular proprioception, which translates mechanical cell deformation into adaptive cytoskeletal dynamics. We excluded classical integrin-based mechanotransduction because we observed $T_{RM}$ polarization in the absence of specific integrin ligands, as well as on pluronic-passivated surfaces containing polystyrene (PS) beads (fig. S5C). Various mammalian and nonmammalian cell types subjected to spatial confinement use their nuclei to measure absolute environmental dimensions (*29*, *30*). According to this "nuclear ruler" model, confinement-induced mechanical stretching of the nuclear envelope (NE) leads to activation of $Ca^{2+}$-dependent cytosolic phospholipase A2 (PLA2) enzymes (*62*). The resulting production of AA leads to membrane recruitment and activation of MYH9, which, in turn, stimulates sustained actomyosin contraction, bleb formation, and motility (*29*, *30*), which are hallmarks of SMG $T_{RM}$ migration observed here.

To examine whether SMG $T_{RM}$ co-opted the nucleus as mechanosensory organelle for spontaneous migration under confinement, we analyzed nuclear shape under 0.5% agarose confinement. These data confirmed that $T_{RM}$ nuclei became stretched, as reflected by increased maximal cross-sectional area and lower heights (Fig. 4, A and B). To directly establish a link between mechanical cell deformation, cell morphometry, and motility, we used confinement chambers with defined heights to induce nuclear compression without interfering with protrusion formation (Fig. 4C). At a 7-μm chamber height, $T_{RM}$ became trapped without substantial nuclear compression. Under these conditions, $T_{RM}$ remained immotile and round, forming only sparse protrusions (Fig. 4D). In contrast, $T_{RM}$ placed in 4-μm-high chambers acquired a highly polarized cell shape with multiple protrusions that correlated with

Downloaded from https://www.science.org at Harvard University on January 04, 2024

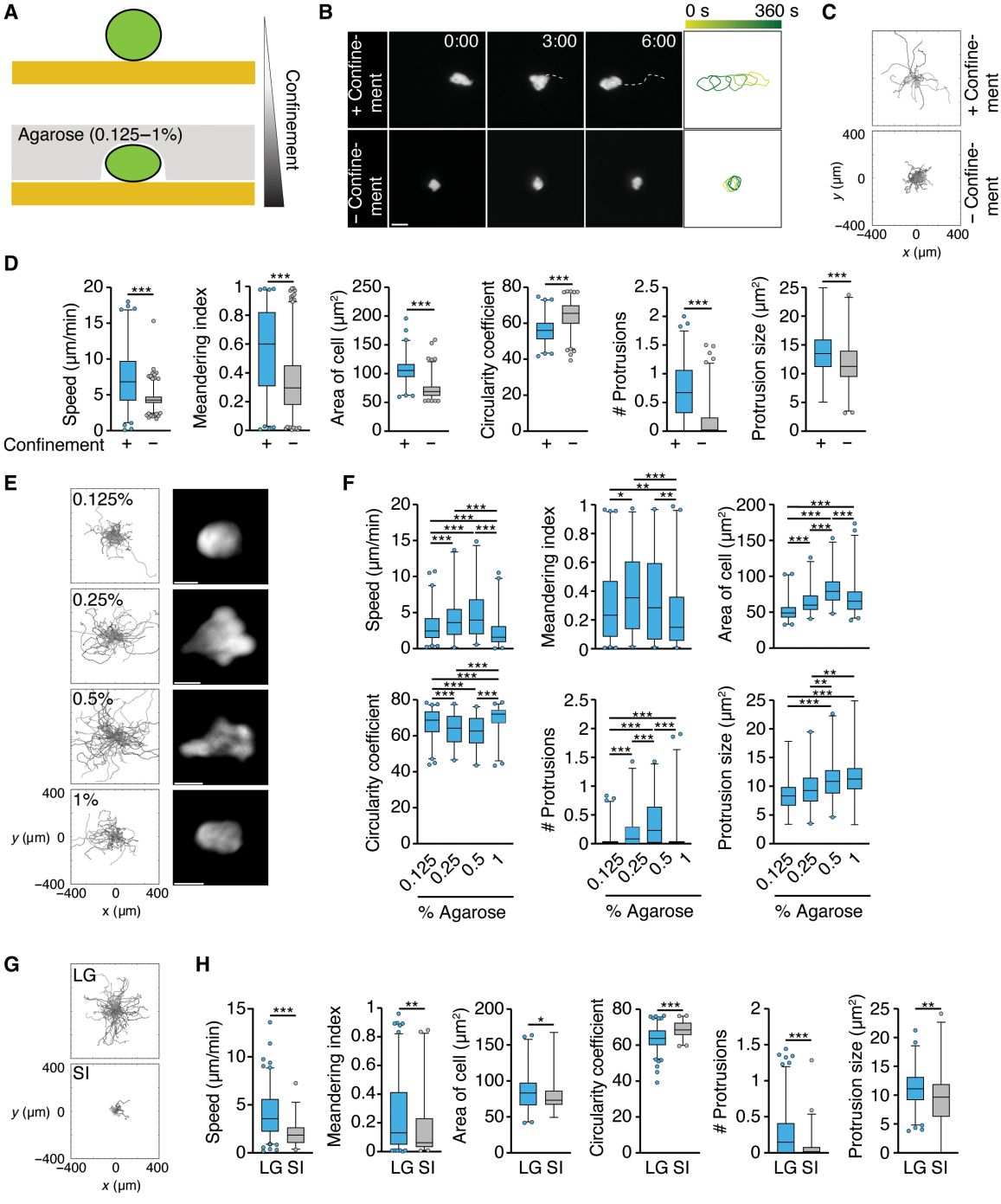


**Fig. 3. Exocrine gland $T_{RM}$ react to mechanical load of their environment with motility.** (**A**) Experimental layout. (**B**) Wide-field fluorescence microscopy images of SMG $T_{RM}$ migrating without or with confinement. (**C**) Exemplary tracks. (**D**) Dynamic and morphometric analysis of $T_{RM}$ motility with or without confinement. Scale bar, 10 µm. (**E**) Exemplary tracks and wide-field fluorescence microscopy images of SMG $T_{RM}$ migrating under distinct mechanical load. Scale bars, 5 µm. (**F**) Dynamic and morphometric analysis of $T_{RM}$ motility under distinct mechanical load. (**G** and **H**) Exemplary tracks (G) and dynamic and morphometric analysis of lacrimal gland (LG) and small intestine (SI) $T_{RM}$ motility (H) on HSA-coated plates under confinement. Data in (D) ($n = 454$ to 1000 tracks), (F) ($n = 159$ to 323 tracks), and (H) ($n = 68$ to 242 tracks) were pooled from at least two independent experiments and analyzed using a Student's *t* test or Mann-Whitney test (D and H) or a Kruskal-Wallis test between all columns (F). $*P < 0.05$, $**P < 0.01$, and $***P < 0.001$.

the induction of spontaneous motility (Fig. 4D and movie S11). To examine whether mechanosensing-triggered motility can also be induced in other T cell subsets at a distinct confinement threshold, we placed SMG $T_{RM}$ or $T_N$ in 2- and 4-µm-high chambers. In contrast to $T_{RM}$, $T_N$ did not display spontaneous motility at 4-µm confinement, whereas both cell populations failed to migrate under 2-µm confinement, accompanied by signs of cell death (fig. S6, A and B). Thus, in the experimental conditions used here, we

Downloaded from https://www.science.org at Harvard University on January 04, 2024

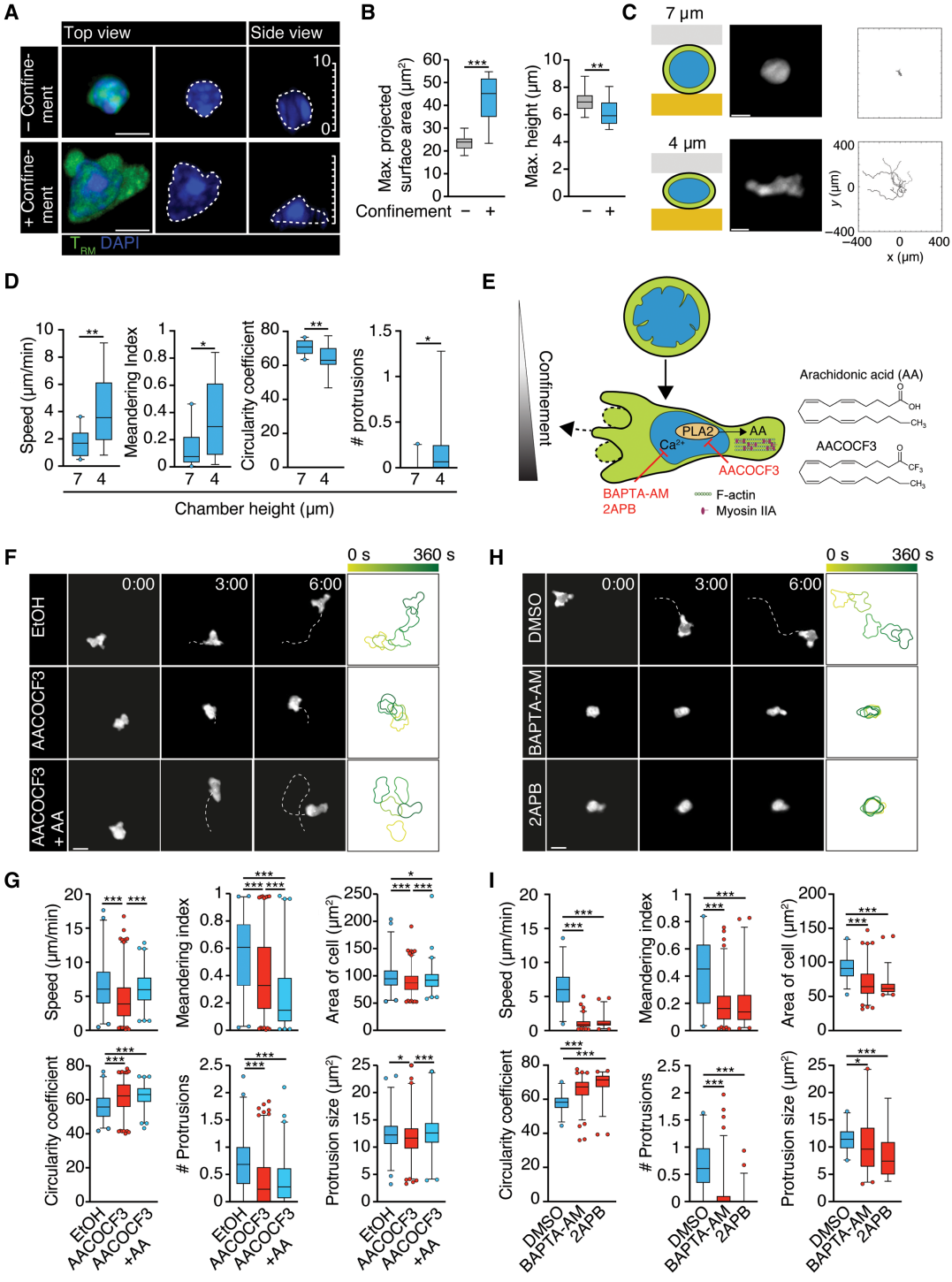


**Fig. 4. Confinement-induced nuclear deformation correlates with $Ca^{2+}$ and AA-dependent autonomous SMG $T_{RM}$ motility.** (**A**) Confocal image of nuclear deformation in under-agarose confinement. Scale bars, 5 µm. (**B**) Projected maximum cross-sectional area and maximum nuclear height with and without confinement ($n = 20$ to 23 nuclei). (**C**) Schematic layout, micrograph, and exemplary tracks of SMG $T_{RM}$ in the confinement chamber. Scale bars, 5 µm. (**D**) Dynamic and morphometric analysis of $T_{RM}$ motility in confinement chambers. (**E**) Scheme of confinement-induced nuclear stretching and selected inhibitors of evasive reflex mediated by $Ca^{2+}$ flux from intracellular stores, induction of PLA2 activity, and release of arachidonic acid (AA). 2APB, BAPTA-AM, and the AA analog AACOCF3 are inhibitors of intracellular $Ca^{2+}$ channels, intracellular $Ca^{2+}$, and PLA2 activity, respectively. (**F**) Wide-field fluorescence microscopy images of SMG $T_{RM}$ under agarose migration in the presence of AACOCF3 and AA. Time in min:s. Scale bar, 10 µm. (**G**) Dynamic and morphometric analysis of $T_{RM}$ motility in the presence of AACOCF3 and AA. (**H**) Wide-field fluorescence microscopy images of SMG $T_{RM}$ under agarose migration in the presence of BAPTA-AM and 2ABP. Time in min:s. Scale bar, 10 µm. (**I**) Dynamic and morphometric analysis of $T_{RM}$ motility under agarose in the presence of BAPTA-AM and 2ABP. Data in (D) ($n = 35$ to 43 tracks), (G) ($n = 296$ to 708 tracks), and (I) ($n = 63$ to 199 tracks) were pooled from at least two independent experiments and analyzed using Student's *t* test and Mann-Whitney test (D) or Kruskal-Wallis against control (G and I). $*P < 0.05$, $**P < 0.01$, and $***P < 0.001$.

Downloaded from https://www.science.org at Harvard University on January 04, 2024

could not induce $T_{RM}$-like motility in $T_N$ isolated from lymphoid tissue.

To further corroborate the link between nuclear deformation and confinement-induced $T_{RM}$ motility, we used the AA analog AACOCF3 as an inhibitor of PLA2 and other AA-producing enzymes (Fig. 4E) (*29*). In under-agarose assays, AACOCF3 treatment led to decreased $T_{RM}$ speeds, as well as reduced directionality and number and size of leading edge protrusions (Fig. 4, F and G, and movie S12). Addition of excess AA to AACOCF3-treated $T_{RM}$ rescued SMG $T_{RM}$ speeds, cell spreading, and protrusion sizes. AA-treated $T_{RM}$ cells frequently changed direction, resulting in a low meandering index (Fig. 4, F and G, and movie S12). These data suggest that although SMG $T_{RM}$ are able to respond to external AA, this treatment affects the preservation of stable polarity. We examined whether other T cell populations responded similarly to AA stimulation. Whereas the addition of AA slightly increased chemokinetic $T_N$ speeds (from 0.6 to 1.5 μm/min), this effect was much lower compared with the impact of CCL21, suggesting that AA is not sufficient to induce robust motility in these cells. Along the same line, AACOCF3 treatment did not impair CCL21-induced $T_N$ motility, whereas it partially reduced CXCL10-induced $T_{RM}$ speeds and directionality (fig. S6, C and D).

In addition to AA production, nuclear mechanosensing requires generation of an intracellular $Ca^{2+}$ flux, whereas extracellular $Ca^{2+}$ is not required (*29*, *30*). To address the role for intracellular $Ca^{2+}$ sensing, we blocked intracellular $Ca^{2+}$ by 1,2-bis(2-aminophenoxy) ethane-*N*,*N*,*N*′,*N*′-tetraacetic acid–acetoxymethyl (BAPTA-AM). In parallel, we added 2-aminoethoxydiphenylborane (2APB) to inhibit stretch-sensitive channels, such as inositol triphosphate receptors (InsP3R), which liberate $Ca^{2+}$ from NE and perinuclear endoplasmic reticulum membranes. Both inhibitors resulted in strongly decreased $T_{RM}$ speeds, directionality, cell polarization, and protrusion formation (Fig. 4H and I, and movie S13). Together, confinement-induced SMG $T_{RM}$ migration is susceptible to inhibitors of the nuclear mechanosensing module (*29*, *30*).

Next, we analyzed whether $T_{RM}$ expressed candidate factors involved in nuclear mechanosensing (Fig. 4E). The ubiquitously expressed family member cPLA2a (encoded by *Pla2g4a*) has been implicated in regulating the mechanosensitive response in dendritic cells (DCs) and other cell types (*29*, *30*, *62*). However, mining the ImmGen database (www.immgen.org/) showed low to absent *Pla2g4a* expression in T cells except for double-negative thymocytes, which we confirmed by quantitative polymerase chain reaction analysis (fig. S7, A and B). For increased sensitivity, we performed a "NanoString" multiplex gene expression analysis of factors potentially involved in the mechanosensitive response by comparing sorted $T_N$, $T_{CM}$, $T_{EM}$, and SMG $T_{RM}$ OT-I T cells. First, we validated the sorting strategy by confirming subset-specific marker detection (fig. S7C). Although this sensitive approach corroborated low to absent *Pla2g4a* expression in T cells, we detected the expression of *Pla2g4b*, *Pla2g10*, *Pla2g12a*, and *Pla2g15* in $T_{RM}$ (fig. S7D). SMG $T_{RM}$ also expressed stretch-activated InsP3Rs, which are involved in intracellular $Ca^{2+}$ release upon nuclear compression (fig. S7E) (*29*, *63*). We did not detect noticeable differences between memory T cell subset expression of factors regulating NE structure, including lamin A/C, lamin B receptor, and emerin, as well as members of the linker of nucleoskeleton and cytoskeleton complex Sun1/2 and nesprins 1 to 4 (fig. S7, F and G). Together, $T_{RM}$ express several $Ca^{2+}$ channels and PLA2 isoforms that might contribute to mechanosensing.

## Mechanosensing-induced $T_{RM}$ motility enhances target cell interception

We designed an in vitro system to examine the impact of $T_{RM}$ mechanosensing on target cell encounter as a simplified tissue surveillance test. We placed SMG $T_{RM}$ with a majority of unpulsed B cells spiked with rare cognate pMHC-pulsed, fluorescently labeled B cells in under-agarose confinement (Fig. 5A). In this system, $T_{RM}$ need to actively migrate to identify dispersed target cells among an excess of bystander cells. $T_{RM}$ were actively scanning B cells for the presence of cognate pMHC (movie S14). Within the observation period, almost half of the control $T_{RM}$ (47%) were able to identify and engage with at least one target cell during the observation period, with 8% of $T_{RM}$ interacting with four or more targets (Fig. 5, B and C). Many interactions were short-lived and resulted in cell death as assessed by dye leakage (movie S14). Addition of the PLA2 inhibitor AACOCF3 disrupted the "search and destroy" pattern (Fig. 5B), with only 32 and 2% of $T_{RM}$ engaged with more than one and a maximum of four targets, respectively (Fig. 5C). In sum, confinement-induced random motility enhances the ability of $T_{RM}$ to efficiently track and eliminate dispersed target cells.

Downloaded from https://www.science.org at Harvard University on January 04, 2024

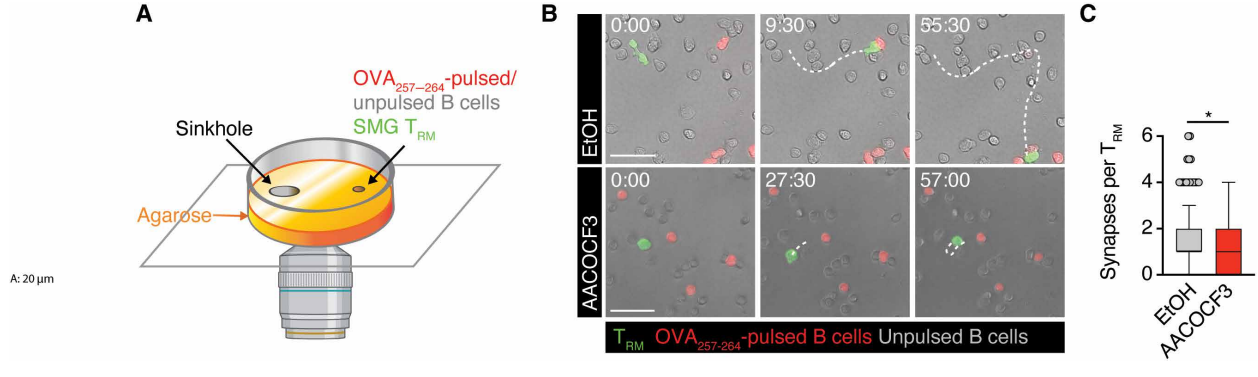


**Fig. 5. Blocking mechanosensing impairs $T_{RM}$ target cell identification.** (**A**) Experimental layout. (**B**) Wide-field fluorescence microscopy images of confined SMG $T_{RM}$ tracking of dispersed target cells with and without AACOCF3. Time in min:s. Scale bars, 30 μm. (**C**) Quantification of $T_{RM}$ – target B cell synapse formation with or without AACOCF3. Data in (C) ($n$ = 139 to 341 synapses) were pooled from two independent experiments and analyzed by Mann-Whitney test. *$P < 0.05$.

### In vivo interference with mechanosensing impairs SMG $T_{RM}$ surveillance

We set out to expand our in vitro observations to tissue surveillance in vivo. Confocal analysis confirmed nuclear deformation occurring in SMG $T_{RM}$ within dense secretory epithelium-rich tissue (Fig. 6A). To examine nuclear mechanosensing-triggered pathways during homeostatic SMG surveillance, we used two-photon intravital microscopy (2PM) to quantify baseline OT-I $T_{RM}$ motility parameters in LCMV-OVA–immunized SMGs before overlaying 20 or 50 μM BAPTA-AM on the SMG preparation for 20 min and recording $T_{RM}$ motility for additional 1 to 4 hours (Fig. 6B and movie S15). BAPTA-AM has been reported to accumulate efficiently in cells in vivo (*64*). Accordingly, the short BAPTA-AM superfusion caused a dose-dependent decrease in SMG $T_{RM}$ speeds and directionality (Fig. 6, C to F), with a concomitant increase in arrest coefficients and sphericity (Fig. 6, F and G). These observations are consistent with the pronounced inhibition of $T_{RM}$ migration by intracellular $Ca^{2+}$ chelation in under-agarose assays (Fig. 4, H and I).

Last, we examined whether mechanosensing contributes to SMG $T_{RM}$ surveillance in response to a local virus rechallenge. We administered an attenuated murine cytomegalovirus (MCMV)–3D-ΔvRAP strain expressing mCherry and the $OVA_{257–264}$ peptide epitope into SMGs via the Wharton's duct of LCMV-OVA–immunized mice in the memory phase, as described (*26*). Recipient mice were subsequently treated with dimethyl sulfoxide (DMSO) or AACOCF3 for 68 hours after MCMV infection (Fig. 6H). We chose AACOCF3 over BAPTA-AM to avoid an impact on $T_{RM}$ function resulting from impaired intracellular $Ca^{2+}$ flux. Intravital imaging confirmed that immediately after AACOCF3 treatment of LCMV-OVA–memory mice, the SMG $T_{RM}$ scanning behavior was disrupted as measured by a drop in directionality, although speeds were not significantly affected in the conditions used here (fig. S8, A and B). This may reflect the weaker in vitro inhibition by AACOCF3 as compared with $Ca^{2+}$ chelators (Fig. 4F). After MCMV infection via the Wharton's duct, we administered anti-α4 and $\alpha_L$ (LFA-1)–blocking monoclonal antibodies (mAbs) to prevent recruitment of circulating T cells without affecting interstitial $T_{RM}$ motility (*26*). Neither administration of AACOCF3 over 3 days alone or in combination with anti-α4 and LFA-1 blocking mAbs had a notable effect on total $T_{RM}$ numbers or their CD69 and CD103 expression (fig. S8, C and D). In control experiments, MCMV-3D-ΔvRAP infection into one SMG lobe did not yield a significant increase in $T_{RM}$ numbers as compared to uninfected contralateral lobes (fig. S8, E and F), irrespective of treatment with anti-α4 and LFA-1 integrin mAbs or the lymphocyte-sequestering drug FTY720 (fig. S8, F and G). These data suggested no or only limited local proliferation of SMG $T_{RM}$ or T cell recruitment during rechallenge with the attenuated MCMV strain used here. In accordance, we observed only few $mCherry^+$ MCMV-infected cells in control- and AACOCF3-treated SMG sections at 68 hours p.i. (fig. S8H), in line with the key role for tissue-resident macrophages for clearance of infected cells (*26*). Consistent with these observations, a histological analysis of MCMV-challenged SMG sections on day 3 p.i. showed comparable numbers of SMG $T_{RM}$ in control- and AACOCF3-treated recipients (Fig. 6, J and I). In contrast, when we examined $T_{RM}$ distribution as a readout for inflammation-induced T cell accumulation, we observed an average of 10.5 ± 4.6 $T_{RM}$ clusters/section (mean ± SEM; median, 4.8) in control-treated SMGs, with $T_{RM}$ accumulating both in $EpCAM^{high}$ epithelial tubes and $EpCAM^{low}$ acini (Fig. 6, I and K). In contrast, $T_{RM}$ clustering in infected SMG was substantially reduced to 1.9 ± 1.9 clusters (median 1.3) in AACOCF3-treated recipients (Fig. 6, I and K). Together, these data support a role for mechanosensing for $T_{RM}$ tissue surveillance of exocrine glands as a complementary mechanism to canonical motility driven by biochemical cues (Fig. 6L) (*29*, *30*, *65*, *66*).

## DISCUSSION

$CD8^+$ $T_{RM}$ surveil organs with diverse tissue architectures, cellular and extracellular matrix compositions, and varying degrees of microbial exposure. Conceivably, organ surveillance is accomplished by local adaptations of their patrolling modus to enable efficient cell scanning and interception of viral infections. In epithelial barriers that are constitutively exposed to microbes, chemokines and integrin ligands contribute to $T_{RM}$ surveillance (*6*–*12*). Here, we report that exocrine gland $T_{RM}$ have the capacity of spontaneous F-actin treadmilling, which endows them with an internal force generation module that bypasses the requirement for chemoattractant and adhesion receptor sensing. Instead, a mechanosensing module allows these cells to measure the degree of confinement-induced mechanical load. This module is coupled to a promigratory response and is susceptible to inhibitors of the nuclear mechanogauge, implying a nongenetic function of the nucleus in this process. Thus, in these nonbarrier organs with low constitutive chemokine expression (*27*), memory T cell subsets are equipped to sense and react to the physical properties of their tissue of residence, extracting promigratory cues from spatial confinement for baseline surveillance. At the same time, they retain their chemosensing capacity to complement their protective function during infection, suggesting a multitiered surveillance strategy.

Amoeboid cell migration is based on continuous polymerization of F-actin at the leading edge and contraction of F-actin filaments by myosin motors at the trailing edge of the cell (*48*). Depending on the cell type examined, amoeboid migration spans a continuum from mostly Rho-driven actomyosin contractility-driven (as in some DCs) to mostly Rac-driven motility lacking protrusions (as in $T_N$) (*23*, *42*). Our data suggest that SMG $T_{RM}$ acquire a blend of these migration modes, presumably as an adaptation to the confined microenvironment of exocrine glands (*26*). Our data further indicate that mechanical load is sufficient to trigger exocrine gland $T_{RM}$ polarization and motility, accompanied by increased cortical actomyosin contractility. Mechanosensing is increasingly acknowledged to play a central role in the immune system (*67*–*70*). On a molecular level, T cells use their TCR as a mechanosensitive receptor to gauge pMHC affinity and for target cell elimination, in a process called mechanosurveillance (*71*, *72*). In the innate immune system, mechanical cues detected by Piezo1 ion channels in macrophages contribute to lung inflammation (*73*), and subsets of spleen DCs use adhesion G protein–coupled receptors as cues for proper positioning close to venous sinusoids (*74*). In motile $T_{RM}$, mechanosensing is susceptible to pharmacological inhibitors of signaling pathways induced by nuclear compression. Until recently, the nucleus has been mainly considered as a passive storage for genetic information. Furthermore, as the cell's biggest organelle, the nucleus constitutes a major obstacle to cellular passage through constricted spaces (*75*). However, recent findings in DC and other leukocytes have uncovered a central role for the nucleus in selecting the migratory path by determining

Downloaded from https://www.science.org at Harvard University on January 04, 2024

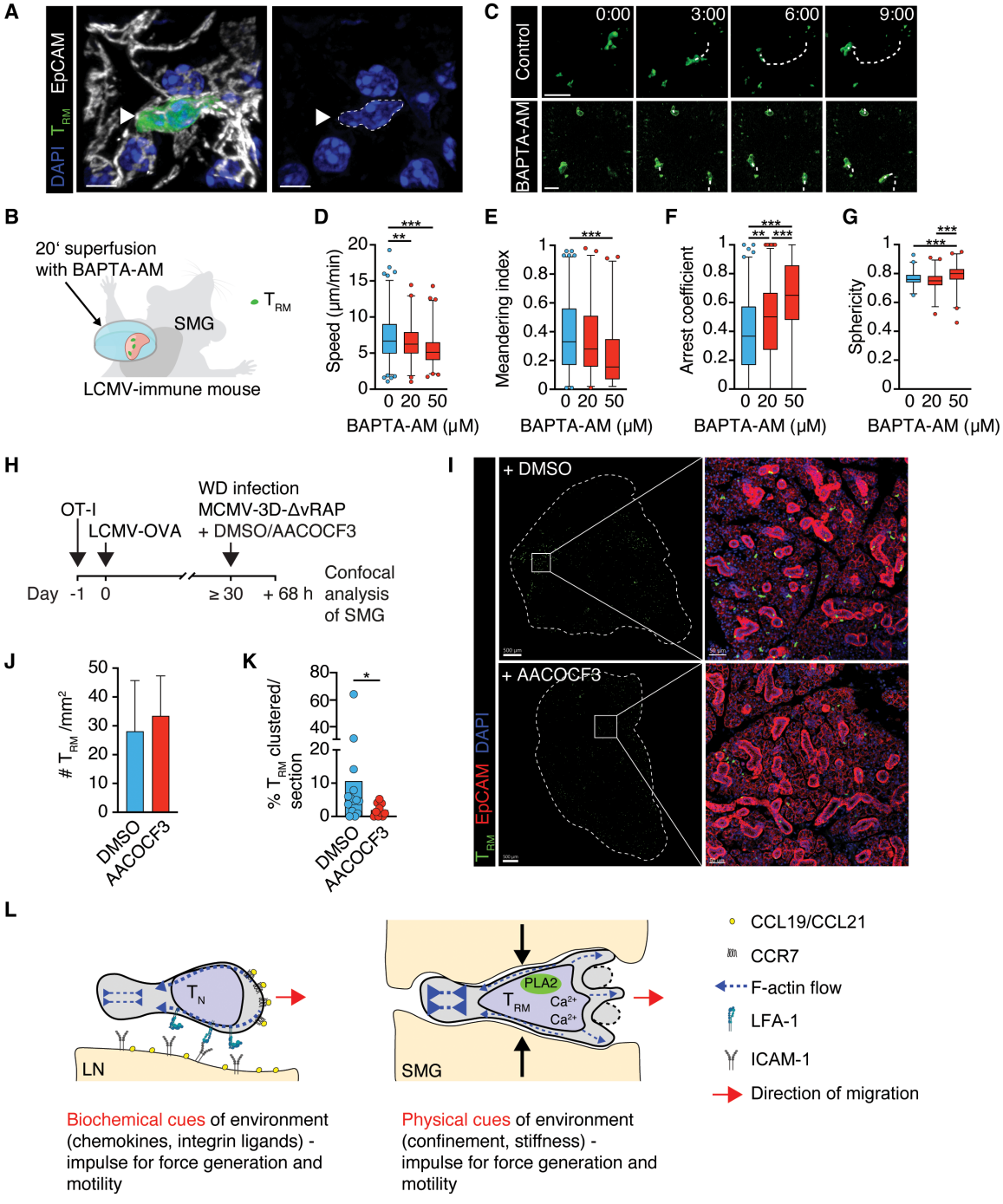


**Fig. 6. Blocking mechanosensing disrupts invivo SMG $T_{RM}$ migration.** (**A**) Confocal image of SMG $T_{RM}$ (arrowhead) in situ. Scale bars, 5 µm. (**B**) Scheme of BAPTA-AM superfusion. (**C**) 2PM images of SMG $T_{RM}$ migration before (baseline) and after 50 µM BAPTA-AM superfusion. Scale bars, 10 µm. (**D** to **G**) Speeds (D), meandering index (E), arrest coefficient (F), and sphericity (G) of $T_{RM}$ before and 1 to 4 hours after superfusion with BAPTA-AM. (**H**) Experimental layout of MCMV-3D-ΔvRAP rechallenge. (**I**) Confocal sections of MCMV-challenged SMGs in control (DMSO)– and AACOCF3-treated recipients. The dotted line marks the outline of SMG section; the square depicts insert. Scale bar, 500 and 50 (insert) µm. (**J**) Number of $T_{RM}$ per area in control- and AACOCF3-treated SMGs. (**K**) Percent of clustered $T_{RM}$ in control- and AACOCF3-treated recipients in 10 to 14 sections from three independent experiments ($n = 24$ control- and AACOCF3-treated mice in total). (**L**) Graphical summary. Data in (D to G) ($n = 207$ to 323 tracks) and (J and K) are pooled from at least two experiments and analyzed using Kruskal-Wallis (D to G), Student's $t$ test (J), or Mann-Whitney test (K). $^*P < 0.05$, $^{**}P < 0.01$, and $^{***}P < 0.001$.

permissive pore sizes (*76*). In line with these findings, the nucleus also serves as a central element for cellular proprioception. Much like humans sense and react to their environment through sight, hearing, touch, smell, and taste, recent studies have provided compelling evidence for nuclear deformation and an autonomous contractile response as the cellular correlate of space and pressure

Downloaded from https://www.science.org at Harvard University on January 04, 2024

sensing (*65*, *77*). To accomplish this feat, the nucleus measures absolute dimensions through the stretching of its NE, beyond which a cell-specific set point triggers an "evasive reflex" via increased cortical contractility and spontaneous cell translocation (*29*, *30*). Given its low constitutive membrane trafficking, the quiescent NE is particularly suited as low noise detector to convert mechanical perturbations into chemical signals as compared with plasma membranes, which display rapid turnover (*78*).

To date, the precise factors generating AA and other signals involved in nuclear mechanosensing are not well characterized owing to the complex cell type–specific regulation of lipid metabolism and $Ca^{2+}$ channel expression (*79*–*81*). As an example, the cPLA2a isoform, which has been implicated in regulating the contractile response in DCs and zebrafish progenitor stem cells (*29*, *30*, *82*), is absent or only expressed at very low levels in mature T cells. Together with the fact that compensatory mechanisms between different isoforms might occur, genetic approaches to disrupt mechanosensing in $T_{RM}$ constitute a formidable challenge. Although many cell types display a $Ca^{2+}$ and PLA2-mediated response upon nuclear disturbance (*29*, *30*, *62*), our data suggest that mechanosensing-driven motility is not a universal feature of all T cell subsets, at least not in the experimental conditions applied here. Thus, $T_N$, $T_{CM}$, and $T_{RM}$ lodged in gut and skin epithelium do not spontaneously move when placed under confinement (*26*). For the latter population, this may reflect their greater dependence on $G\alpha_i$-coupled signaling as compared with exocrine $T_{RM}$ (*8*). Local chemokines induced by constant microbial exposure might help avoid accidental egress of epithelial $T_{RM}$ outside the host by restricting them in close vicinity to the basement membrane. In turn, mechanosensing-triggered motility for baseline surveillance might be preferentially induced in tissues with limited microbial exposure, where steady-state chemokine levels are low (*27*). This surveillance strategy equips $T_{RM}$ with flexibility to surveil multiple organs with diverse cellular and matrix composition, while retaining responsiveness to inflammation-triggered local chemokine gradients.

As a limitation, despite providing solid evidence for mechanosensing capacities in $T_{RM}$ subsets, the molecular pathways involved in this process remain undefined. Furthermore, the use of pharmacological inhibitors to interfere with confinement-induced $T_{RM}$ motility might affect additional signaling pathways in these cells or influence bystander cells in in vivo experiments. Along the same line, the in vivo pharmacokinetics of the PLA2 and $Ca^{2+}$ flux inhibitors are not well defined, rendering an assessment of the degree of inhibition after administration difficult. Last, our study does not address to which extent mechanosensing is a property shared with other leukocytes, such as natural killer cells lodged in exocrine glands.

In sum, although it is well established that the transition of $T_N$ to $T_{EFF}$ and memory T cell subsets is accompanied by changes in the chemoattractant and adhesion receptor repertoire, our data suggest that these changes do not fully explain the scanning behavior of these cells in distinct organs. Thus, physical properties of the tissue of residency are integrated by adaptive immune cells with local biochemical cues for a specific multitier immune surveillance strategy. It is conceivable that mechanosensing elicits site-specific signaling and epigenetic and metabolic adaptations in local immune cell populations, encouraging further investigation into the underlying molecular regulation.

## MATERIALS AND METHODS

### Study design

The aim of this study was to examine the mechanisms underlying intrinsic motility of SMG $T_{RM}$. To this end, we systemically administered LCMV-OVA and isolated Ag-specific $CD8^+$ T cells from SMG and other organs. We applied ex vivo migration assays, immunofluorescence, intravital imaging, gene expression analysis, and flow cytometry to compare their migration requirements with $CD8^+$ $T_N$. Furthermore, we administered pharmacological inhibitors of small guanosine triphosphatase and nuclear mechanosensing signaling pathways to functional assays. Last, we assessed the role of the $T_{RM}$ mechanosensing module for target finding and cell clustering after viral rechallenge. Mice or isolated T cells were randomly assigned to experimental groups and analyzed without excluding outliers, and experimenters were not blinded. The numbers of independent experiments are indicated in the figure legends.

### Mice

Tg(TcraTcrb)1100Mjb ("OT-I") TCR transgenic mice (*31*) were backcrossed to C57BL/6-Tg(CAG-EGFP)1Osb/J ("$GFP^+$") (*83*), hCD2-dsRed ("$dsRed^+$") (*84*), tdTomato-expressing Ai14 × ZP3 ("$tdTom^+$") (*85*, *86*), mT/mG (*87*), and LifeAct-GFP lines (*33*). $GFP^+$ OT-I were further crossed to CD4-Cre × $MYH9^{flox/flox}$ (*88*), $DOCK2^{-/-}$ (*40*) and $DOCK8^{-/-}$ (*89*) lines, and $dsRed^+$ OT-I to the MYH9-GFP reporter line (*49*). DOCK2-GFP was described before (*90*). All mice were bred at the animal facility of the University of Bern and the University of Fribourg, Switzerland and were used as lymphocyte donor mice. Six- to 10-week-old male and female sex-matched C57BL/6JRj mice (Janvier, Le Genest-Saint-Isle, France) were used as recipient mice. All experiments were performed in accordance to federal animal experimentation regulations and approved by the cantonal committee.

### T cell transfer and viral infections

$CD8^+$ T cells were negatively isolated from spleen and peripheral LNs using the EasySep Mouse $CD8^+$ T cell Isolation Kit (STEMCELL Technologies) or the MojoSort Mouse $CD8^+$ T cell Isolation Kit (BioLegend) according to the manufacturer's instructions. OT-I T cells ($5 \times 10^4$) were intravenously transferred into recipient mice 24 hours before intraperitoneal infection with $10^5$ plaque-forming units (PFU) LCMV-OVA (*32*).

### Reagents

Sodium pyruvate (P04-43100), Hepes buffer (P05-01100), minimum essential medium nonessential amino acids (P08-32100), L-glutamine (200 mM; P04-80100), and PenStrep (P06-07100) were purchased from PAN-Biotech, and RPMI 1640 (#21875-034) and fetal bovine serum (10270-106) were from Gibco. CPYPP (Tocris) was used at 50 μM; CK666 (R&D), at 100 μM; ML141 (Tocris) and MLCK inhibitor peptide 18 (Calbiochem), at 20 μM; Y27632 (Sigma-Aldrich or Hello Bio), at 20 μM or 200 μg per mouse in vivo; AACOCF3 (Tocris or Enzo Life Sciences), at 20 μM or 300 μg per mouse in vivo; BAPTA-AM (Cayman Chemical), at 10 μM; AA (Cayman Chemical), at 70 μM; 2APB (Tocris), at 100 μM; W56/F56 (R&D), at 100 μM; and Rhosin (Sigma-Aldrich), at 10 μM.

### Flow cytometry analysis

At indicated time points, single-cell suspensions of spleens, LNs, and SMGs were prepared for flow cytometry as described in the

Downloaded from https://www.science.org at Harvard University on January 04, 2024

Supplementary Materials and acquired on Attune NxT Flow Cytometer (Thermo Fisher Scientific) or LSRFortessa (BD). Data were analyzed with FlowJo.

### Immunofluorescence

OT-I memory cells were isolated from SMGs and spleens of C57BL/6 mice infected with LCMV-OVA at >30 days p.i. Single-cell suspensions of SMGs and spleens were generated as above and sorted for $tdT^+$ T cells. Ibidi sticky slides (untreated side) with a 12-well removable chamber were coated with fibronectin (10 μg/ml; Sigma-Aldrich). Cells were added and incubated for 2 hours at 37°C, fixed with 4% paraformaldehyde for 20 min at room temperature (RT), washed, and permeabilized using BD Fixation/Permeabilization solution 20 min at 4°C. Cells were blocked with BD Perm/Wash 2% goat serum for 1 hour at RT, stained with rabbit anti-pMLC (Cell Signaling Technology, 3674) overnight at 4°C, washed, stained with a goat anti-rabbit AF647 (Invitrogen, A32733) for 1 hour at RT, and washed again. The 12-well removable chamber was removed, and the sticky slide was mounted on a glass slide with Prolong Gold Antifade with DAPI (Thermo Fisher Scientific) and let dry at RT for 24 hours. Images were taken with a Leica SP5 confocal microscope using a 63× glycerin objective [APO CS, numerical aperture (NA) 1.3]. Data were analyzed with Imaris (Bitplane). For SMG sections, SMGs were frozen in optimal cutting temperature (OCT) and cryosectioned for immunofluorescence (6 or 10 μm), followed by labeling with goat anti-GFP (Rockland, 600-101-215) and anti-EpCAM AF647 (BioLegend, 118212) for epithelium.

### 2PM image acquisition and analysis

2PM intravital imaging of SMGs was performed as described in (*91*) and in the Supplementary Materials. ImSpector software was used to control the 2PM system and to acquire images with an automated system providing real-time drift correction (*92*). Data were analyzed with Imaris (Bitplane) and a customized script for arrest coefficient analysis with a threshold of 4 μm/min as described (*26*).

### Under-agarose and confinement chamber assays

$T_N$ were isolated from spleen and PLN of a naive mouse using the EasySep Mouse $CD8^+$ T cell Isolation Kit (STEMCELL Technologies) or the MojoSort Mouse $CD8^+$ T cell Isolation Kit (BioLegend) according to the manufacturer's instructions. $T_{RM}$ were isolated from SMGs, LGs, or SIs of C57BL/6 mice infected by LCMV-OVA for >30 days by flow cytometry sorting. Under-agarose assays were performed as described in (*26*) and in the Supplementary Materials. For target cell engagement experiments, $2 \times 10^4$ SMG $T_{RM}$ were mixed with $0.2 \times 10^6$ 1 nM $OVA_{257–264}$-pulsed B cells isolated using the EasySep Mouse B cell Isolation Kit (STEMCELL Technologies) and labeled with 2.5 μM (5-(and-6)-(((4-chloromethyl)benzoyl) amino)tetramethylrhodamine) (CMTMR) together with $1 \times 10^6$ unpulsed, nonlabeled B cells in the presence of B cell-activating factor of the tumour-necrosis-factor family (BAFF) (100 ng/ml; R&D Systems, 8876-BF-010). Time-lapse images were taken from the center of the dish using a Zeiss fluorescent microscope (Axio Observer, Zeiss) or a GE DeltaVision Elite wide-field fluorescent microscope (U plan, S Apo, NA 0.75). Images were taken every 20 s for 15 to 20 min. For the TIRF images, the GE DeltaVision microscope was used with a laser module and a 60× TIRF objective.

A Dynamic Cell Confiner device (4Dcell, France) was used to study $T_{RM}$ cell migration under defined chamber heights. Polydimethylsiloxane suction cups with 4- or 7-μm-high micropillars were prepared as described in the manufacturer's instructions. Plates were coated with 2% HSA. Sorted SMG $T_{RM}$ ($10^5$ cells) were transferred into each plate. Before imaging, the suction cup was plugged to an adjustable vacuum source. Once confined at a pressure from −50 to −100 mbar, cells were imaged with a GE DeltaVision microscope as above.

### Dynamic and morphometric cell analysis

Cortical F-actin flow in TIRF image sequences was measured using the Imaris (Bitplane) particle tracking function to generate tracks of $GFP^+$ F-actin speckles, as previously described (*35*, *36*, *93*). The global speed depicts displacement over tracking time for each track. Morphometric data were analyzed with Imaris or a custom-made FIJI plugin (source code is available at https://github.com/Matthieu-Palayret/DynMorpho_Analysis; fig. S2). For dynamic and morphometric cell analysis, cell contours were determined using the ADAPT plugin (*94*). For each trajectory, the dynamic and morphometric analysis consisted of calculating six outputs: the average speed of the cell; the meandering index of the trajectory, which is a measure of its linearity, calculated as the ratio of the distance separating the initial and final points of the trajectory over the distance traveled by the cell (the ratio equals 1 if the trajectory is exactly linear); the average area of the cell; its average circularity coefficient, calculated as the average over the trajectory of the ratio of the true area of the cell over the area of a circular cell that would have the same perimeter ($=4\pi \times \text{area/perimeter}^2$ − the coefficient equals 100 when the cell is perfectly circular); and both the average number and size of the protrusions of the cell (the uropod being excluded) over its whole trajectory.

### 3D collagen matrix migration

$T_{RM}$ migration through a confined 3D collagen type I matrix was performed in μ-Slide Chemotaxis ibiTreat chambers (ibidi, Switzerland) as described (*95*). Briefly, sorted LifeAct-GFP × mT/mG $T_{RM}$ were resuspended at $5 \times 10^5$ cells/ml in RPMI 1640 medium supplemented with 10% heat-inactivated fetal bovine serum. PureCol collagen I (30 μl; CellSystems, Troisdorf, Germany), 4 μl of 10× DMEM, and 2 μl of 7.5% $NaHCO_3$ were premixed, carefully mixed with 18 μl of cell suspension, and applied to μ-Slide Chemotaxis chambers. Collagen was allowed to polymerize for 40 min at 37°C in a humidified incubator. Live cell imaging was performed on a laser scanning microscope (Leica TCS SP5; Leica, Switzerland) using an HCX PL APO CS 63.0× (NA 1.40) oil ultraviolet objective at 0.65-s intervals on a microscope stage fitted with a Tokai Hit Thermo Plate at 37°C.

### MCMV rechallenge and cluster analysis

MCMV rechallenge experiments were performed as described (*26*). Briefly, $GFP^+$ OT-I cells ($5 \times 10^4$ per mouse) were transferred into C57BL/6 mice and intraperitoneally infected on the following day with $10^5$ PFU of LCMV-OVA. At >30 days p.i., mice were treated with vehicle (DMSO) or 300 μg of AACOCF3, together with anti-α4 (clone PS/2) and anti-$\alpha_L$ (LFA-1; clone FD441.8; each 100 μg per mouse) mAbs (*26*). After 2 hours, $10^6$ PFU of the attenuated MCMV-3D-ΔvRAP strain expressing the SIINFEKL peptide epitope (*96*) were locally administered to the right SMG via Wharton's duct injection. Recipient mice were treated every 12 hours with 300 μg of AACOCF3

Downloaded from https://www.science.org at Harvard University on January 04, 2024

or vehicle (final volume, 100 µl in saline) and at 48 hours p.i. again with PS/2 and FD441.8 as above. Alternatively, we administered FTY720 (2 µg/g body weight) daily. On day 3 (68 hours after MCMV injection), mice were perfused with 4% paraformaldehyde (PFA), and the right SMG was harvested, fixed overnight at 4°C in 5 ml of 4% PFA/phosphate-buffered saline, transferred into 30% sucrose, and kept at 4°C for 24 hours. SMGs were frozen in OCT and cryosectioned for immunofluorescence (6 or 10 µm), followed by labeling with goat anti-GFP (Rockland, 600-101-215) and donkey anti-goat AF488 (Thermo Fisher Scientific, A11055), and rabbit anti–red fluorescent protein (Abcam, ab62341), and donkey anti-rabbit AF555 (Thermo Fisher Scientific, A32794) for viral foci. Tile scans were obtained by wide-field (DeltaVision) or confocal (Leica STELLARIS Falcon 8) fluorescence microscopy, and $T_{RM}$ were identified using the Imaris "spots" function. Nine neighbor clusters were empirically defined by choosing a maximum distance of 62 µm between spots. The percentage of clustered cells was obtained by dividing the number of clustered over total number of spots.

### Statistical analysis

Two-tailed, unpaired Student's *t* test, Mann-Whitney *U* test, one-way analysis of variance (ANOVA) with Dunn's multiple comparisons test, Kruskal-Wallis test, or a Wilcoxon rank test was used to determine statistical significance (Prism, GraphPad). Whiskers in box-and-whisker plots depict a range of 90 to 100% of individual values (nonincluded values are shown as individual dots), whereas the box comprises 50% of all data points and the line within the box displaying the median. Significance was set at $P < 0.05$.

## Supplementary Materials

**This PDF file includes:**
Material and Methods
Figs. S1 to S8

**Other Supplementary Material for this manuscript includes the following:**
Movies S1 to S15
Data file S1
MDAR Reproducibility Checklist

## REFERENCES AND NOTES


1. J. W. Griffith, C. L. Sokol, A. D. Luster, Chemokines and chemokine receptors: Positioning cells for host defense and immunity. *Annu. Rev. Immunol.* **32**, 659–702 (2014).
2. J. V. Stein, N. Ruef, Regulation of global CD8+ T-cell positioning by the actomyosin cytoskeleton. *Immunol. Rev.* **289**, 232–249 (2019).
3. D. Masopust, J. M. Schenkel, The integration of T cell migration, differentiation and function. *Nat. Rev. Immunol.* **13**, 309–320 (2013).
4. J. R. Groom, Regulators of T-cell fate: Integration of cell migration, differentiation and function. *Immunol. Rev.* **289**, 101–114 (2019).
5. D. J. Fowell, M. Kim, The spatio-temporal control of effector T cell migration. *Nat. Rev. Immunol.* **21**, 582–596 (2021).
6. N. Iijima, A. Iwasaki, Tissue instruction for migration and retention of TRM cells. *Trends Immunol.* **36**, 556–564 (2015).
7. S. N. Mueller, L. K. Mackay, Tissue-resident memory T cells: Local specialists in immune defence. *Nat. Rev. Immunol.* **16**, 79–89 (2016).
8. A. Zaid, J. L. Hor, S. N. Christo, J. R. Groom, W. R. Heath, L. K. Mackay, S. N. Mueller, Chemokine receptor–dependent control of skin tissue–resident memory T cell formation. *J. Immunol.* **199**, 2451–2459 (2017).
9. P. C. Rosato, L. K. Beura, D. Masopust, Tissue resident memory T cells and viral immunity. *Curr. Opin. Virol.* **22**, 44–50 (2017).
10. P. A. Szabo, M. Miron, D. L. Farber, Location, location, location: Tissue resident memory T cells in mice and humans. *Sci. Immunol.* **4**, eaas9673 (2019).
11. S. C. Sasson, C. L. Gordon, S. N. Christo, P. Klenerman, L. K. Mackay, Local heroes or villains: Tissue-resident memory T cells in human health and disease. *Cell. Mol. Immunol.* **17**, 113–122 (2020).
12. S. K. Bromley, H. Akbaba, V. Mani, R. Mora-Buch, A. Y. Chasse, A. Sama, A. D. Luster, CD49a regulates cutaneous resident memory CD8+ T cell persistence and response. *Cell Rep.* **32**, 108085 (2020).
13. M. Heeg, A. W. Goldrath, Insights into phenotypic and functional CD8+ TRM heterogeneity. *Immunol. Rev.* **316**, 8–22 (2023).
14. P. Friedl, B. Weigelin, Interstitial leukocyte migration and immune function. *Nat. Immunol.* **9**, 960–969 (2008).
15. T. Lämmermann, M. Sixt, Mechanical modes of 'amoeboid' cell migration. *Curr. Opin. Cell Biol.* **21**, 636–644 (2009).
16. D. L. Bodor, W. Pönisch, R. G. Endres, E. K. Paluch, Of cell shapes and motion: The physical basis of animal cell migration. *Dev. Cell* **52**, 550–562 (2020).
17. E. K. Paluch, I. M. Aspalter, M. Sixt, Focal adhesion-independent cell migration. *Annu. Rev. Cell Dev. Biol.* **32**, 469–490 (2016).
18. L. K. Fritz-Laylin, The evolution of animal cell motility. *Curr. Biol.* **30**, R477–R482 (2020).
19. S. SenGupta, C. A. Parent, J. E. Bear, The principles of directed cell migration. *Nat. Rev. Mol. Cell Biol.* **22**, 529–547 (2021).
20. T. Okada, J. G. Cyster, CC chemokine receptor 7 contributes to gi-dependent T cell motility in the lymph node. *J. Immunol.* **178**, 2973–2978 (2007).
21. T. Worbs, T. R. Mempel, J. Bölter, U. H. von Andrian, R. Förster, CCR7 ligands stimulate the intranodal motility of T lymphocytes in vivo. *J. Exp. Med.* **204**, 489–495 (2007).
22. M. Faroudi, M. Hons, A. Zachacz, C. Dumont, R. Lyck, J. V. Stein, V. L. J. Tybulewicz, Critical roles for Rac GTPases in T-cell migration to and within lymph nodes. *Blood* **116**, 5536–5547 (2010).
23. M. Hons, A. Kopf, R. Hauschild, A. Leithner, F. Gaertner, J. Abe, J. Renkawitz, J. V. Stein, M. Sixt, Chemokines and integrins independently tune actin flow and substrate friction during intranodal migration of T cells. *Nat. Immunol.* **19**, 606–616 (2018).
24. E. Woolf, I. Grigorova, A. Sagiv, V. Grabovsky, S. W. Feigelson, Z. Shulman, T. Hartmann, M. Sixt, J. G. Cyster, R. Alon, Lymph node chemokines promote sustained T lymphocyte motility without triggering stable integrin adhesiveness in the absence of shear forces. *Nat. Immunol.* **8**, 1076–1085 (2007).
25. R. T. Boscacci, F. Pfeiffer, K. Gollmer, A. I. C. Sevilla, A. M. Martin, S. F. Soriano, D. Natale, S. Henrickson, U. H. von Andrian, Y. Fukui, M. Mellado, U. Deutsch, B. Engelhardt, J. V. Stein, Comprehensive analysis of lymph node stroma-expressed Ig superfamily members reveals redundant and nonredundant roles for ICAM-1, ICAM-2, and VCAM-1 in lymphocyte homing. *Blood* **116**, 915–925 (2010).
26. B. Stolp, F. Thelen, X. Ficht, L. M. Altenburger, N. Ruef, V. V. G. K. Inavalli, P. Germann, N. Page, F. Moalli, A. Raimondi, K. A. Keyser, S. M. S. Jafari, F. Barone, M. S. Dettmer, D. Merkler, M. Iannacone, J. Sharpe, C. Schlapbach, O. T. Fackler, U. V. Nägerl, J. V. Stein, Salivary gland macrophages and tissue-resident CD8+ T cells cooperate for homeostatic organ surveillance. *Sci. Immunol.* **5**, eaaz4371 (2020).
27. C. E. Hughes, R. J. B. Nibbs, A guide to chemokines and their receptors. *FEBS J.* **285**, 2944–2971 (2018).
28. A. Reversat, F. Gaertner, J. Merrin, J. Stopp, S. Tasciyan, J. Aguilera, I. de Vries, R. Hauschild, M. Hons, M. Piel, A. Callan-Jones, R. Voituriez, M. Sixt, Cellular locomotion using environmental topography. *Nature* **582**, 582–585 (2020).
29. A. J. Lomakin, C. J. Cattin, D. Cuvelier, Z. Alraies, M. Molina, G. P. F. Nader, N. Srivastava, P. J. Sáez, J. M. Garcia-Arcos, I. Y. Zhitnyak, A. Bhargava, M. K. Driscoll, E. S. Welf, R. Fiolka, R. J. Petrie, N. S. D. Silva, J. M. González-Granado, N. Manel, A. M. Lennon-Duménil, D. J. Müller, M. Piel, The nucleus acts as a ruler tailoring cell responses to spatial constraints. *Science* **370**, eaba2894 (2020).
30. V. Venturini, F. Pezzano, F. C. Castro, H.-M. Häkkinen, S. Jiménez-Delgado, M. Colomer-Rosell, M. Marro, Q. Tolosa-Ramon, S. Paz-López, M. A. Valverde, J. Weghuber, P. Loza-Alvarez, M. Krieg, S. Wieser, V. Ruprecht, The nucleus measures shape changes for cellular proprioception to control dynamic cell behavior. *Science* **370**, eaba2644 (2020).
31. K. A. Hogquist, S. C. Jameson, W. R. Heath, J. L. Howard, M. J. Bevan, F. R. Carbone, T cell receptor antagonist peptides induce positive selection. *Cell* **76**, 17–27 (1994).
32. S. M. Kallert, S. Darbre, W. V. Bonilla, M. Kreutzfeldt, N. Page, P. Müller, M. Kreuzaler, M. Lu, S. Favre, F. Kreppel, M. Löhning, S. A. Luther, A. Zippelius, D. Merkler, D. D. Pinschewer, Replicating viral vector platform exploits alarmin signals for potent CD8+ T cell-mediated tumour immunotherapy. *Nat. Commun.* **8**, 15327 (2017).
33. J. Riedl, A. H. Crevenna, K. Kessenbrock, J. H. Yu, D. Neukirchen, M. Bista, F. Bradke, D. Jenne, T. A. Holak, Z. Werb, M. Sixt, R. Wedlich-Söldner, Lifeact: A versatile marker to visualize F-actin. *Nat. Methods* **5**, 605–607 (2008).
34. A. Babich, S. Li, R. S. O'Connor, M. C. Milone, B. D. Freedman, J. K. Burkhardt, F-actin polymerization and retrograde flow drive sustained PLCγ1 signaling during T cell activation. *J. Cell Biol.* **197**, 775–787 (2012).
35. A. T. Ritter, Y. Asano, J. C. Stinchcombe, N. M. G. Dieckmann, B.-C. Chen, C. Gawden-Bone, S. van Engelenburg, W. Legant, L. Gao, M. W. Davidson, E. Betzig, J. Lippincott-Schwartz, G. M. Griffiths, Actin depletion initiates events leading to granule secretion at the immunological synapse. *Immunity* **42**, 864–876 (2015).
36. W. A. Comrie, A. Babich, J. K. Burkhardt, F-actin flow drives affinity maturation and spatial organization of LFA-1 at the immunological synapse. *J. Cell Biol.* **208**, 475–491 (2015).


Downloaded from https://www.science.org at Harvard University on January 04, 2024

37. M. Bajénoff, J. G. Egen, L. Y. Koo, J. P. Laugier, F. Brau, N. Glaichenhaus, R. N. Germain, Stromal cell networks regulate lymphocyte entry, migration, and territoriality in lymph nodes. *Immunity* **25**, 989–1001 (2006).
38. J. Renkawitz, K. Schumann, M. Weber, T. Lämmermann, H. Pflicke, M. Piel, J. Polleux, J. P. Spatz, M. Sixt, Adaptive force transmission in amoeboid cell migration. *Nat. Cell Biol.* **11**, 1438–1443 (2009).
39. D. Bray, J. G. White, Cortical flow in animal cells. *Science* **239**, 883–888 (1988).
40. Y. Fukui, O. Hashimoto, T. Sanui, T. Oono, H. Koga, M. Abe, A. Inayoshi, M. Noda, M. Oike, T. Shirai, T. Sasazuki, Haematopoietic cell-specific CDM family protein DOCK2 is essential for lymphocyte migration. *Nature* **412**, 826–831 (2001).
41. A. Leithner, A. Eichner, J. Müller, A. Reversat, M. Brown, J. Schwarz, J. Merrin, D. J. J. de Gorter, F. Schur, J. Bayerl, I. de Vries, S. Wieser, R. Hauschild, F. P. L. Lai, M. Moser, D. Kerjaschki, K. Rottner, J. V. Small, T. E. B. Stradal, M. Sixt, Diversified actin protrusions promote environmental exploration but are dispensable for locomotion of leukocytes. *Nat. Cell Biol.* **18**, 1253–1259 (2016).
42. P. Vargas, P. Maiuri, M. Bretou, P. J. Sáez, P. Pierobon, M. Maurin, M. Chabaud, D. Lankar, D. Obino, E. Terriac, M. Raab, H.-R. Thiam, T. Brocker, S. M. Kitchen-Goosen, A. S. Alberts, P. Sunareni, S. Xia, R. Li, R. Voituriez, M. Piel, A.-M. Lennon-Duménil, Innate control of actin nucleation determines two distinct migration behaviours in dendritic cells. *Nat. Cell Biol.* **18**, 43–53 (2016).
43. L. K. Fritz-Laylin, S. J. Lord, R. D. Mullins, WASP and SCAR are evolutionarily conserved in actin-filled pseudopod-based motility. *J. Cell Biol.* **216**, 1673–1688 (2017).
44. A. Nishikimi, T. Uruno, X. Duan, Q. Cao, Y. Okamura, T. Saitoh, N. Saito, S. Sakaoka, Y. Du, A. Suenaga, M. Kukimoto-Niino, K. Miyano, K. Gotoh, T. Okabe, F. Sanematsu, Y. Tanaka, H. Sumimoto, T. Honma, S. Yokoyama, T. Nagano, D. Kohda, M. Kanai, Y. Fukui, Blockade of inflammatory responses by a small-molecule inhibitor of the Rac activator DOCK2. *Chem. Biol.* **19**, 488–497 (2012).
45. B. J. Nolen, N. Tomasevic, A. Russell, D. W. Pierce, Z. Jia, C. D. McCormick, J. Hartman, R. Sakowicz, T. D. Pollard, Characterization of two classes of small molecule inhibitors of Arp2/3 complex. *Nature* **460**, 1031–1034 (2009).
46. H. Jiang, F. Pan, L. M. Erickson, M.-S. Jang, T. Sanui, Y. Kunisaki, T. Sasazuki, M. Kobayashi, Y. Fukui, Deletion of DOCK2, a regulator of the actin cytoskeleton in lymphocytes, suppresses cardiac allograft rejection. *J. Exp. Med.* **202**, 1121–1130 (2005).
47. Q. Zhang, C. G. Dove, J. L. Hor, H. M. Murdock, D. M. Strauss-Albee, J. A. Garcia, J. N. Mandl, R. A. Grodick, H. Jing, D. B. Chandler-Brown, T. E. Lenardo, G. Crawford, H. F. Matthews, A. F. Freeman, R. J. Cornall, R. N. Germain, S. N. Mueller, H. C. Su, DOCK8 regulates lymphocyte shape integrity for skin antiviral immunity. *J. Exp. Med.* **211**, 2549–2566 (2014).
48. K. M. Yamada, M. Sixt, Mechanisms of 3D cell migration. *Nat. Rev. Mol. Cell. Biol.* **20**, 738–752 (2019).
49. Y. Zhang, M. A. Conti, D. Malide, F. Dong, A. Wang, Y. A. Shmist, C. Liu, P. Zerfas, M. P. Daniels, C.-C. Chan, E. Kozin, B. Kachar, M. J. Kelley, J. B. Kopp, R. S. Adelstein, Mouse models of MYH9-related disease: Mutations in nonmuscle myosin II-A. *Blood* **119**, 238–250 (2012).
50. A. Zehrer, R. Pick, M. Salvermoser, A. Boda, M. Miller, K. Stark, L. T. Weckbach, B. Walzog, D. Begandt, A fundamental role of Myh9 for neutrophil migration in innate immunity. *J. Immunol.* **201**, 1748–1764 (2018).
51. M. Vicente-Manzanares, X. Ma, R. S. Adelstein, A. R. Horwitz, Non-muscle myosin II takes centre stage in cell adhesion and migration. *Nat. Rev. Mol. Cell Biol.* **10**, 778–790 (2009).
52. T. Isogai, R. van der Kammen, M. Innocenti, SMIFH2 has effects on Formins and p53 that perturb the cell cytoskeleton. *Sci. Rep.* **5**, 9802 (2015).
53. Y. Nishimura, S. Shi, F. Zhang, R. Liu, Y. Takagi, A. D. Bershadsky, V. Viasnoff, J. R. Sellers, The formin inhibitor, SMIFH2, inhibits members of the myosin superfamily. *J. Cell Sci.* **134**, jcs253708 (2021).
54. T. F. Robertson, P. Chengappa, D. G. Atria, C. F. Wu, L. Avery, N. H. Roy, I. Maillard, R. J. Petrie, J. K. Burkhardt, Lymphocyte egress signal sphingosine-1-phosphate promotes ERM-guided, bleb-based migration. *J. Cell Biol.* **220**, e202007182 (2021).
55. P. Kameritsch, J. Renkawitz, Principles of leukocyte migration strategies. *Trends. Cell. Biol.* **30**, 818–832 (2020).
56. A. Smith, P. Stanley, K. Jones, L. Svensson, A. McDowall, N. Hogg, The role of the integrin LFA-1 in T-lymphocyte migration. *Immunol. Rev.* **218**, 135–146 (2007).
57. T. Wolf, W. Jin, G. Zoppi, I. A. Vogel, M. Akhmedov, C. K. E. Bleck, T. Beltraminelli, J. C. Rieckmann, N. J. Ramirez, M. Benevento, S. Notarbartolo, D. Bumann, F. Meissner, B. Grimbacher, M. Mann, A. Lanzavecchia, F. Sallusto, I. Kwee, R. Geiger, Dynamics in protein translation sustaining T cell preparedness. *Nat. Immunol.* **21**, 927–937 (2020).
58. A. D. Weems, E. S. Welf, M. K. Driscoll, F. Y. Zhou, H. Mazloom-Farsibaf, B.-J. Chang, V. S. Murali, G. M. Gihana, B. G. Weiss, J. Chi, D. Rajendran, K. M. Dean, R. Fiolka, G. Danuser, Blebs promote cell survival by assembling oncogenic signalling hubs. *Nature* **615**, 517–525 (2023).
59. A. Smith, Y. R. Carrasco, P. Stanley, N. Kieffer, F. D. Batista, N. Hogg, A talin-dependent LFA-1 focal zone is formed by rapidly migrating T lymphocytes. *J. Cell Biol.* **170**, 141–151 (2005).
60. P. R. O'Neill, J. A. Castillo-Badillo, X. Meshik, V. Kalyanaraman, K. Melgarejo, N. Gautam, Membrane flow drives an adhesion-independent amoeboid cell migration mode. *Dev. Cell* **46**, 9–22.e4 (2018).
61. L. Aoun, A. Farutin, N. Garcia-Seyda, P. Nègre, M. S. Rizvi, S. Tlili, S. Song, X. Luo, M. Biarnes-Pelicot, R. Galland, J.-B. Sibarita, A. Michelot, C. Hivroz, S. Rafai, M.-P. Valignat, C. Misbah, O. Theodoly, Amoeboid swimming is propelled by molecular paddling in lymphocytes. *Biophys. J.* **119**, 1157–1177 (2020).
62. B. Enyedi, M. Jelcic, P. Niethammer, The cell nucleus serves as a mechanotransducer of tissue damage-induced inflammation. *Cell* **165**, 1160–1170 (2016).
63. A. Selezneva, A. J. Gibb, D. Willis, The nuclear envelope as a regulator of immune cell function. *Front. Immunol.* **13**, 842269 (2022).
64. M. Tymianski, M. C. Wallace, I. Spigelman, M. Uno, P. L. Carlen, C. H. Tator, M. P. Charlton, Cell-permeant Ca2+ chelators reduce early excitotoxic and ischemic neuronal injury in vitro and in vivo. *Neuron* **11**, 221–235 (1993).
65. Z. Shen, P. Niethammer, A cellular sense of space and pressure. *Science* **370**, 295–296 (2020).
66. J. T. Long, J. Lammerding, Nuclear deformation lets cells gauge their physical confinement. *Dev. Cell.* **56**, 156–158 (2021).
67. M. Huse, Mechanical forces in the immune system. *Nat. Rev. Immunol.* **17**, 679–690 (2017).
68. S. V. Pageon, M. A. Govendir, D. Kempe, M. Biro, Mechanoimmunology: Molecular-scale forces govern immune cell functions. *Mol. Biol. Cell* **29**, 1919–1926 (2018).
69. M. Chabaud, N. Paillon, K. Gaus, C. Hivroz, Mechanobiology of antigen-induced T cell arrest. *Biol. Cell* **112**, 196–212 (2020).
70. H. Du, J. M. Bartleson, S. Butenko, V. Alonso, W. F. Liu, D. A. Winer, M. J. Butte, Tuning immunity through tissue mechanotransduction. *Nat. Rev. Immunol.* **23**, 174–188 (2023).
71. R. Basu, B. M. Whitlock, J. Husson, A. L. Floc'h, W. Jin, A. Oyler-Yaniv, F. Dotiwala, G. Giannone, C. Hivroz, N. Biais, J. Lieberman, L. C. Kam, M. Huse, Cytotoxic T cells use mechanical force to potentiate target cell killing. *Cell* **165**, 100–110 (2016).
72. M. Tello-Lafoz, K. Srpan, E. E. Sanchez, J. Hu, J. Remsik, Y. Romin, A. Calò, D. Hoen, U. Bhanot, L. Morris, A. Boire, K. C. Hsu, J. Massagué, M. Huse, E. E. Er, Cytotoxic lymphocytes target characteristic biophysical vulnerabilities in cancer. *Immunity* **54**, 1037–1054.e7 (2021).
73. A. G. Solis, P. Bielecki, H. R. Steach, L. Sharma, C. C. D. Harman, S. Yun, M. R. de Zoete, J. N. Warnock; S. D. F. To, A. G. York, M. Mack, M. A. Schwartz, Charles. S. D. Cruz, N. W. Palm, R. Jackson, R. A. Flavell, Mechanosensation of cyclical force by PIEZO1 is essential for innate immunity. *Nature* **573**, 69–74 (2019).
74. D. Liu, L. Duan, L. B. Rodda, E. Lu, Y. Xu, J. An, L. Qiu, F. Liu, M. R. Looney, Z. Yang, C. D. C. Allen, Z. Li, A. Marson, J. G. Cyster, CD97 promotes spleen dendritic cell homeostasis through the mechanosensing of red blood cells. *Science* **375**, eabi5965 (2022).
75. T. Lämmermann, B. L. Bader, S. J. Monkley, T. Worbs, R. Wedlich-Söldner, K. Hirsch, M. Keller, R. Förster, D. R. Critchley, R. Fässler, M. Sixt, Rapid leukocyte migration by integrin-independent flowing and squeezing. *Nature* **453**, 51–55 (2008).
76. J. Renkawitz, A. Kopf, J. Stopp, I. de Vries, M. K. Driscoll, J. Merrin, R. Hauschild, E. S. Welf, G. Danuser, R. Fiolka, M. Sixt, Nuclear positioning facilitates amoeboid migration along the path of least resistance. *Nature* **568**, 546–550 (2019).
77. Y. Kalukula, A. D. Stephens, J. Lammerding, S. Gabriele, Mechanics and functional consequences of nuclear deformations. *Nat. Rev. Mol. Cell. Biol.* **23**, 583–602 (2022).
78. B. Enyedi, P. Niethammer, A case for the nuclear membrane as a mechanotransducer. *Cell. Mol. Bioeng.* **9**, 247–251 (2016).
79. J. B. Park, C. S. Lee, J.-H. Jang, J. Ghim, Y.-J. Kim, S. You, D. Hwang, P.-G. Suh, S. H. Ryu, Phospholipase signalling networks in cancer. *Nat. Rev. Cancer* **12**, 782–792 (2012).
80. C. C. Leslie, Cytosolic phospholipase $A_2$: Physiological function and role in disease. *J. Lipid Res.* **56**, 1386–1402 (2015).
81. F. Fenninger, W. A. Jefferies, What's bred in the bone: Calcium channels in lymphocytes. *J. Immunol.* **202**, 1021–1030 (2019).
82. Z. Alraies, C. A. Rivera, M.-G. Delgado, D. Sanséau, M. Maurin, R. Amadio, G. M. Piperno, G. Dunsmore, A. Yatim, L. L. Mariano, P. J. Sáez, M. Gratia, O. Lamiable, A. Moreau, A. Williart, B. Albaud, P. Legoix, H. Nakano, D. N. Cook, T. Lawrence, N. Manel, F. Benvenuti, F. Ginhoux, H. D. Moreau, G. P. F. Nader, M. Piel, A.-M. Lennon-Duménil, A shape sensing mechanism driven by Arp2/3 and cPLA2 licenses dendritic cells for migration to lymph nodes in homeostasis. bioRxiv 10.1101/2022.08.09.503223 [Preprint] (2023).
83. B. C. Schaefer, M. L. Schaefer, J. W. Kappler, P. Marrack, R. M. Kedl, Observation of antigen-dependent CD8+ T-cell/ dendritic cell interactions in vivo. *Cell. Immunol.* **214**, 110–122 (2001).
84. A. C. Kirby, M. C. Coles, P. M. Kaye, Alveolar macrophages transport pathogens to lung draining lymph nodes. *J. Immunol.* **183**, 1983–1989 (2009).
85. W. N. de Vries, L. T. Binns, K. S. Fancher, J. Dean, R. Moore, R. Kemler, B. B. Knowles, Expression of Cre recombinase in mouse oocytes: A means to study maternal effect genes. *Genesis* **26**, 110–112 (2000).
86. L. Madisen, T. A. Zwingman, S. M. Sunkin, S. W. Oh, H. A. Zariwala, H. Gu, L. L. Ng, R. D. Palmiter, M. J. Hawrylycz, A. R. Jones, E. S. Lein, H. Zeng, A robust and high-


Downloaded from https://www.science.org at Harvard University on January 04, 2024

throughput Cre reporting and characterization system for the whole mouse brain. *Nat. Neurosci.* **13**, 133–140 (2010).
87. M. D. Muzumdar, B. Tasic, K. Miyamichi, L. Li, L. Luo, A global double-fluorescent Cre reporter mouse. *Genesis* **45**, 593–605 (2007).
88. J. Jacobelli, R. S. Friedman, M. A. Conti, A.-M. Lennon-Dumenil, M. Piel, C. M. Sorensen, R. S. Adelstein, M. F. Krummel, Confinement-optimized three-dimensional T cell amoeboid motility is modulated via myosin IIA-regulated adhesions. *Nat. Immunol.* **11**, 953–961 (2010).
89. Y. Harada, Y. Tanaka, M. Terasawa, M. Pieczyk, K. Habiro, T. Katakai, K. Hanawa-Suetsugu, M. Kukimoto-Niino, T. Nishizaki, M. Shirouzu, X. Duan, T. Uruno, A. Nishikimi, F. Sanematsu, S. Yokoyama, J. V. Stein, T. Kinashi, Y. Fukui, DOCK8 is a Cdc42 activator critical for interstitial dendritic cell migration during immune responses. *Blood* **119**, 4451–4461 (2012).
90. Y. Kunisaki, A. Nishikimi, Y. Tanaka, R. Takii, M. Noda, A. Inayoshi, K. Watanabe, F. Sanematsu, T. Sasazuki, T. Sasaki, Y. Fukui, DOCK2 is a Rac activator that regulates motility and polarity during neutrophil chemotaxis. *J. Cell Biol.* **174**, 647–652 (2006).
91. X. Ficht, F. Thelen, B. Stolp, J. V. Stein, Preparation of murine submandibular salivary gland for upright intravital microscopy. *J. Vis. Exp.* **215**, 1869–1890 (2018).
92. M. Vladymyrov, J. Abe, F. Moalli, J. V. Stein, A. Ariga, Real-time tissue offset correction system for intravital multiphoton microscopy. *J. Immunol. Methods* **438**, 35–41 (2016).
93. J. Daniel, A. G. Godin, M. Palayret, B. Lounis, L. Cognet, M. Blanchard-Desce, Innovative molecular-based fluorescent nanoparticles for multicolor single particle tracking in cells. *J. Phys. D Appl. Phys.* **49**, 084002 (2016).
94. D. J. Barry, C. H. Durkin, J. V. Abella, M. Way, Open source software for quantification of cell migration, protrusions, and fluorescence intensities. *J. Cell Biol.* **209**, 163–180 (2015).
95. E. U. Allmen, G. P. B. Samson, V. Purvanov, T. Maeda, D. F. Legler, CAL-1 as cellular model system to study CCR7-guided human dendritic cell migration. *Front. Immunol.* **12**, 702453 (2021).
96. S. Halle, K. A. Keyser, F. R. Stahl, A. Busche, A. Marquardt, X. Zheng, M. Galla, V. Heissmeyer, K. Heller, J. Boelter, K. Wagner, Y. Bischoff, R. Martens, A. Braun, K. Werth, A. Uvarovskii, H. Kempf, M. Meyer-Hermann, R. Arens, M. Kremer, G. Sutter, M. Messerle, R. Förster, In vivo killing capacity of cytotoxic T cells is limited and involves dynamic interactions and T cell cooperativity. *Immunity* **44**, 233–245 (2016).

**Acknowledgments:** We thank M. Sixt for critical feedback on the manuscript. **Funding:** This work was funded by Swiss National Foundation (SNF) project grants 31003A_172994, 310030L_197711, and 310030_200406; Sinergia project grant CRSII5_170969 (to J.V.S.); Leopoldina fellowship LPDS 2011-16; and the Deutsche Forschungsgemeinschaft project number 240245660-SFB1129 (project 8) (to B.S.). This work benefited from the BioImage Light Microscopy Facility and Cell Analytics Facility of the University of Fribourg. **Author contributions:** N.R. and J.M.M. performed most experiments and analysis with help from X.F., V.P., S.W., P.P., B.S., F.T., and J.B.d.A. M.P. wrote the script for morphometric analysis, and P.G. provided scripts for in vivo cell tracking. J.A., J.S, D.F.L. and J.V.S. supervised the work. J.V.S. wrote the manuscript with input by all co-authors. **Competing interests:** The authors declare that they have no competing interests. **Data and materials availability:** All data needed to evaluate the conclusions in the paper are present in the paper or the Supplementary Materials, including data file S1. All noncommercial materials used in this study are available from J.V.S.

Submitted 20 June 2022
Resubmitted 14 July 2023
Accepted 9 November 2023
Published 22 December 2023
10.1126/sciimmunol.add5724

Downloaded from https://www.science.org at Harvard University on January 04, 2024

Science Immunology

# Exocrine gland–resident memory CD8+ T cells use mechanosensing for tissue surveillance

Nora Ruef, Jose Martínez Magdaleno, Xenia Ficht, Vladimir Purvanov, Matthieu Palayret, Stefanie Wissmann, Petra Pfenninger, Bettina Stolp, Flavian Thelen, Juliana Barreto de Albuquerque, Philipp Germann, James Sharpe, Jun Abe, Daniel F. Legler, and Jens V. Stein

*Sci. Immunol.* **8** (90), eadd5724. DOI: 10.1126/sciimmunol.add5724

**Editor's summary**

Tissue-resident CD8+ T cells ($T_{RM}$) are constantly surveilling organs and tissues for the presence of uninvited microbes. Previous studies have shown that $T_{RM}$ migration is triggered by signaling via chemoattractant and adhesion molecules, which facilitates rapid detection of infected cells. More recent evidence has indicated that $T_{RM}$ within submandibular salivary glands display different motility patterns exclusive of chemosensing. Ruef *et al.* now show that SMG $T_{RM}$ from virally infected mice display spontaneous retrograde F-actin flow as a means of force-generated translocation. Similar patterns of locomotion were detected in $T_{RM}$ from other exocrine glands and were dependent on the sensing of changes in mechanical loads through signals triggered by nuclear deformation. These findings provide critical insight into how $T_{RM}$ can surveil tissue independent of chemosensing. —Christiana Fogg

**View the article online**
https://www.science.org/doi/10.1126/sciimmunol.add5724
**Permissions**
https://www.science.org/help/reprints-and-permissions

Use of this article is subject to the Terms of service

*Science Immunology* (ISSN 2470-9468) is published by the American Association for the Advancement of Science. 1200 New York Avenue NW, Washington, DC 20005. The title *Science Immunology* is a registered trademark of AAAS.

Copyright © 2023 The Authors, some rights reserved; exclusive licensee American Association for the Advancement of Science. No claim to original U.S. Government Works

Downloaded from https://www.science.org at Harvard University on January 04, 2024